

# Dimensional deformation of sine-Gordon breathers into oscillons

José T. Gálvez Ghersi <sup>1, 2,\*</sup> and Jonathan N. Braden, <sup>1, †</sup>

<sup>1</sup>*Canadian Institute for Theoretical Astrophysics, University of Toronto, 60 St. George Street*

<sup>2</sup>*Universidad de Ingeniería y Tecnología - UTEC, Jr. Medrano Silva 165, Lima - Perú*

(Dated: March 13, 2023)

Oscillons are localized field configurations oscillating in time with lifetimes orders of magnitude longer than their oscillation period. In this paper, we simulate non-travelling oscillons produced by deforming the breather solutions of the sine-Gordon model. Such a deformation treats the dimensionality of the model as a real parameter to produce spherically symmetric oscillons. After considering the post-transient oscillation frequency as a control parameter, we probe the initial parameter space to show how the availability of oscillons depends on the number of spatial dimensions. For small dimensional deformations, our findings are consistent with the lack of a minimal amplitude bound to form oscillons. In  $D \gtrsim 2$  spatial dimensions, we observe solutions undergoing intermittent phases of contraction and expansion in their cores. Knowing that stable and unstable configurations can be mapped to disjoint regions of the breather parameter space, we find that amplitude modulated solutions are located in the middle of both stability regimes. This displays the dynamics of critical behavior for solutions around the stability limit.

## I. INTRODUCTION

Oscillons [1] are a remarkable set of long-lived localized states that oscillate in time. In this context, long-lived means that these have lifetimes orders of magnitude longer than their oscillation period. Such objects are held together by a delicate balance of attractive forces and dispersion preventing them from dilution or collapse. In the early universe cosmology, the production of oscillons at the end of inflation [2] seems to have a wide range of consequences, requiring careful analysis to be confirmed: from their possible connections to dark matter [3, 4] to the production of scalar and tensor gravitational modes [5–8].

An interesting feature of several (but still rare) nonlinear field theories is the existence of infinitely long-lived solutions with nontrivial field profiles, known as solitons and solitary waves. Solitons possess the particular property of persisting after interacting with each other [9]. Some well-known examples of solitons include the breathers of the sine-Gordon (SG) equation [10], kinks of the Korteweg-de Vries (KdV) equation [11], and the bright and dark non-topological solitons of the nonlinear Schrödinger (NLS) equation [12]. With the exception solitary waves, all of these persist upon interaction. Oscillon longevity is, at present, still a mystery despite significant work [4, 13–18]. One way to find explanations for this is to deform infinitely long-lived nonlinear 1D field solutions to produce spherically symmetric oscillons.

The primary objective of this paper is to continuously connect non-travelling oscillons with the one-dimensional SG model by deforming the sine-Gordon equation to yield the spherically symmetric  $D$ -dimensional Laplacian. Setting the SG breather as an initial state is not only

supported by graphical intuition on how similar the radial structure of breathers and oscillons are. It also means a major simplification when studying the system, since it is well-known that a single parameter is all we need to describe every solution of the SG equation. In the case of the breather, the frequency of oscillation ( $\omega_{\text{ini}}$ ) determines its enclosed energy and all of its geometrical features. Therefore, when the equations of motion are deformed, measuring the post-transient oscillation frequency ( $\omega_{\text{osc}}$ ) as the solution evolves is a natural way to trace the dynamical state of such a connection. Post-transient energy of the solution is another valuable parameter, since it indicates that many breather-like initial conditions form the same oscillon. Although it is important to remark that so far, there is not a unique parameterization that can be used for these purposes [19, 20].

After scanning a sufficiently large portion of the initial parameter space, the connection produces a slowly varying oscillation frequency map (in  $D \lesssim 2$ ). One of the many uses of such a map is to represent the availability of oscillon states given a set of breather-like initial conditions, and the spread of energies/frequencies where these can be found. Dimensional deformations generate several features in the connecting maps: it is possible to confirm the existence of attractors in large portions of parameter space, which is in agreement with the results in [21–23]. Stable oscillons produced by collapsing shells (i.e.,  $0.1 \leq \omega_{\text{ini}}/\mu \lesssim 0.5$ , where  $\mu$  is the characteristic time/length scale of the problem), are far more frequent when the potential energy of the initial conditions exceeds its kinetic energy. Implying that initial phases are also relevant in the formation of stable oscillons. In  $D \lesssim 2$ , modulation in amplitude appears in large sections of the initial parameter space, especially in regions separating stable and unstable solutions. Such solutions are still spatially localized, but the quasibreather expansion suggested in [4, 17] is not valid anymore. Furthermore, their presence suggests that in  $D \gtrsim 2$  dimensions critical behavior exists in the transition from stable to unstable

\* [jgalvezg@utec.edu.pe](mailto:jgalvezg@utec.edu.pe)

† [jbraden@cita.utoronto.ca](mailto:jbraden@cita.utoronto.ca)

regions. That being the case, it is possible to estimate the critical energy for oscillons to form and its dependence on the number of spatial dimensions. In the high-frequency region of the map ( $\omega_{\text{ini}} \lesssim \mu$ ), we notice that oscillons can be well-represented by the initial breathers only in the perturbative regime (i.e., when  $D < 2$ ), which is not only true for changes in the number of spatial dimensions; but also for mild variations in the curvature of the SG potential well centered at zero. Which produces oscillons in one spatial dimension<sup>1</sup>. For dimensional deformations beyond the perturbative regime, breathers may not have sufficient energy to produce oscillons. Therefore, it is necessary to modify the parameterization of initial conditions to compensate for the lack of energy and increase the availability of stable solutions. This is relevant since, in previous work, it has been suggested that the direct application of the numerical dynamic renormalization-group-based method (NDRG) in [24] may be useful to produce a semi-analytic formula to predict oscillon lifetimes. A consequence of this paper is that such an application is not straightforward, since the generation of solutions in  $D \gtrsim 2$  dimensions requires to go beyond the single-parameter description provided by the SG model.

The organization of this manuscript is as follows: in Section II, we describe the dynamical setup used to study the standing oscillons formed by dimensional deformations of the sine-Gordon equation in the perturbative regime and beyond. We also explain the method used to measure the oscillation frequency, which is the control parameter allowing us to compare breathers with oscillons. In Section III, we show that it is only in the perturbative regime where oscillons are well-represented by breathers. We also show how the number of accessible oscillons and the extent of the oscillation frequencies interval change with the number of spatial dimensions. In Section IV, we study the non-perturbative regime of dimensional deformations. For this purpose, we introduce another way to parameterize the breather-like initial conditions to compensate the lack of energy of the single-parameter SG breathers. Both the presence of intermediate states in  $D \gtrsim 2$  spatial dimensions and the energy flows are consistent with the presence of critical behavior. Amplitude modulated solutions describe the dynamics of phase transitions between stable and unstable solutions as the solutions' energy increases or decreases. Moreover, after sampling a sufficiently large number of cases, it is possible to compute the critical energy needed to form oscillons as a function of the number of spatial dimensions. In Section V, we show that the connection between breathers and oscillons in the perturbative regime also extends to potential deformations. To do so, here we deformed the positive sinusoidal into the axion monodromy potential [25–28], which is relevant in inflationary cosmology. In

Section VI, we deform breathers into oscillons throughout a time-dependent transition in the number of spatial dimensions. Introducing the duration of such dimensional transition as an additional parameter. We observe that, for an initially uniform distribution of breather frequencies, the duration does not vary the oscillation frequency range. However, the availability of amplitude modulated solutions increases in the adiabatic limit, where transitions last more than a few oscillations. Finally, in Section VII, we discuss and conclude.

## II. EQUATIONS OF MOTION AND DIAGNOSTIC PARAMETERS

In this paper, we aim to connect breathers with spherically symmetric oscillons produced by deforming the one-dimensional sine-Gordon (SG) model. To do so, our approach is to deform the SG breather directly from its equations of motion, showing the properties of the resulting numerical solutions as functions of its parameters before deformation.

### A. Deforming the equations of motion

To set our conventions, let us first write the SG equation in its Hamiltonian form

$$\frac{d\phi}{dt} = \Pi, \quad (1)$$

$$\frac{d\Pi}{dt} = \frac{\partial^2 \phi}{\partial x^2} - \frac{V_0}{\phi_*} \sin\left(\frac{\phi}{\phi_*}\right). \quad (2)$$

It is important to remember that the one-dimensional sine-Gordon model is integrable, and possesses an infinite hierarchy of conserved charges [29–32] depending on a single parameter. Conventionally, it is always convenient to reparameterize the field and the  $(t, x)$  coordinates as

$$t \rightarrow \bar{t} \equiv \mu t, \quad x \rightarrow \bar{x} \equiv \mu x, \quad (3)$$

$$\phi \rightarrow \bar{\phi} \equiv \frac{\phi}{\phi_*}, \quad \Pi \rightarrow \bar{\Pi} \equiv \frac{\Pi}{\mu \phi_*},$$

in order to cast Eqns. (1) and (2) in their dimensionless versions

$$\frac{d\bar{\phi}}{d\bar{t}} = \bar{\Pi}, \quad (4)$$

$$\frac{d\bar{\Pi}}{d\bar{t}} = \frac{\partial^2 \bar{\phi}}{\partial \bar{x}^2} - \sin \bar{\phi}. \quad (5)$$

after setting  $\mu^2 = V_0/\phi_*^2$ , which has units of mass squared. It is well-known that SG breathers can be interpreted as bound states of a domain wall-antiwall pair perpetually bouncing against each other. Using them as initial conditions is not merely based on our intuition of how similar the breathers' and oscillons' radial profiles are. It is also practical since breathers only need one parameter

<sup>1</sup> By mild potential deformations, we mean corrections leading to potentials with reflection symmetry around  $\phi = 0$ , and with  $V(0) = 0$  as a minimum.

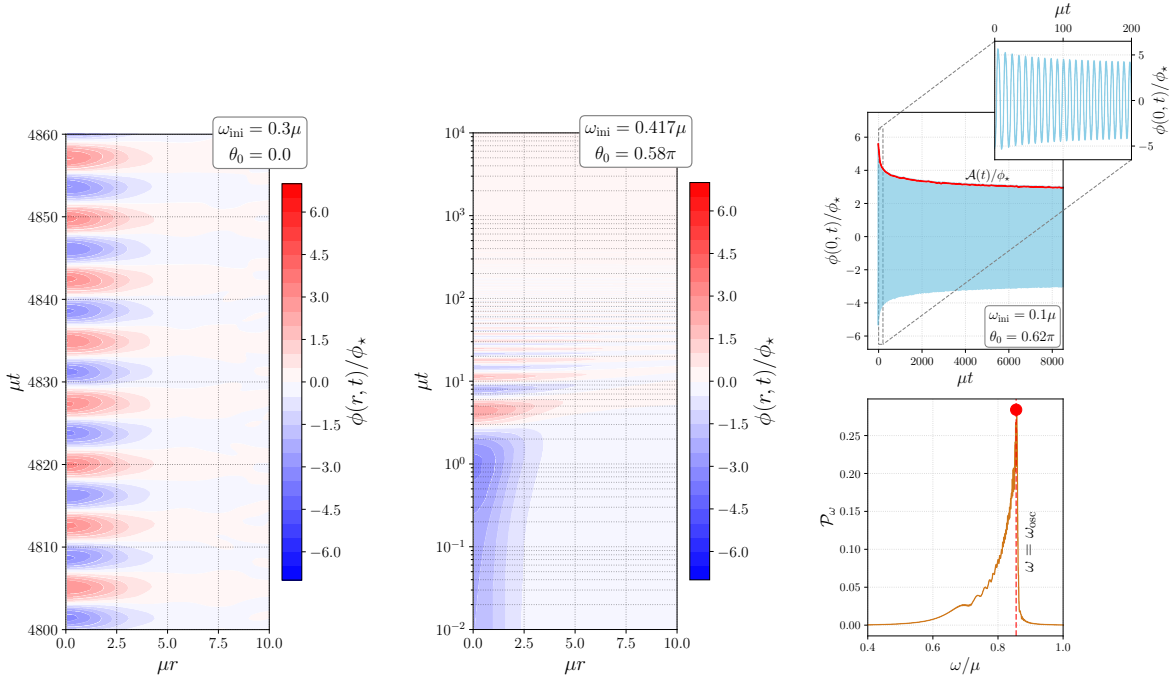


FIG. 1. Showing the spatial structure, time evolution of oscillon cores and determination of the oscillation frequency ( $\omega_{\text{osc}}$ ) for  $\varepsilon = 0.75$ . Left panel: Typical evolution of the radial profile for a long-lived oscillon, deformed from a SG breather with initial frequency  $0.3\mu$  and no phase. Middle panel: Radial profile of a decaying oscillon (observe the time axis in logarithmic scale). Right panel (top): Time evolution of the oscillon evaluated at  $r = 0$  to determine the dominant frequency and the amplitude  $\mathcal{A}$ . Right panel (bottom): From the temporal power spectrum  $\mathcal{P}_\omega$  of the top panel, we determine  $\omega_{\text{osc}}/\mu$  to be the angular frequency with the highest peak (marked by the red dot) in power.

to describe the features of the entire solution, including the infinite tower of conserved quantities. Breathers are solutions of (4) and (5) given

$$\Psi(\bar{x}, \bar{t}) \equiv \frac{\mu \sqrt{1 - \mu^{-2} \omega_{\text{ini}}^2} \cos\left(\frac{\omega_{\text{ini}}}{\mu} \bar{t} - \theta_0\right)}{\omega_{\text{ini}} \cosh(\sqrt{1 - \mu^{-2} \omega_{\text{ini}}^2} \bar{x})}, \quad (6)$$

$$\bar{\phi}(\bar{x}, \bar{t}) = 4 \tan^{-1} \Psi, \quad (7)$$

$$\bar{\Pi}(\bar{x}, \bar{t}) = -\frac{4\mu^{-1} \omega_{\text{ini}} \Psi}{1 + \Psi^2} \tan\left(\frac{\omega_{\text{ini}}}{\mu} \bar{t} - \theta_0\right). \quad (8)$$

Here  $\omega_{\text{ini}}$  is the oscillation frequency of the breather. This parameter not only determines geometrical parameters such as the amplitude, width and energy; but it is also the argument of an infinite hierarchy of conserved charges.  $\theta_0$  corresponds to the phase, fixed as an initial condition. Regularity at the origin demands that the field and conjugate momenta of breathers and oscillons to be even functions of  $\bar{x}$ . It is reasonable to also demand regularity of the oscillons produced by field equations deformations.  $\bar{\Pi}(\bar{x}, \bar{t})$  is the time-derivative of (7), and although its dependence on the tangent function (written in this form just for compactness) it has no singularities.

After switching  $\bar{x}$  to the radial coordinate  $\bar{r}$  (defined in a positive semi-infinite domain), and using the  $D$ -

dimensional Laplacian in spherical symmetry<sup>2</sup>, the equations of motion are given by

$$\frac{d\bar{\Phi}}{d\bar{t}} = \bar{\Pi}_\Phi, \quad (9)$$

$$\frac{d\bar{\Pi}_\Phi}{d\bar{t}} = \left[ \frac{\partial^2}{\partial \bar{r}^2} + \frac{\varepsilon}{\bar{r}} \frac{\partial}{\partial \bar{r}} \right] \bar{\Phi} - \sin \bar{\Phi}, \quad (10)$$

where the term proportional to both  $\varepsilon \equiv D - 1$ . If we use the breathers in (7) and (8) as initial conditions

$$\bar{\Phi}(\bar{r}, 0) = \bar{\phi}(\bar{r}, 0), \quad \bar{\Pi}_\Phi(\bar{r}, 0) = \bar{\Pi}(\bar{r}, 0), \quad (11)$$

and thus, the solutions to the system in Eqs. (9) and (10) are deformations of the SG breather. One of the key parts of our study is to treat the control parameter  $\varepsilon$  as a real input instead of as an integer. In summary, the dimensionless field  $\bar{\Phi}$  in (9, 10) will be written with respect to the original field, i.e.,  $\bar{\Phi} \equiv \phi/\phi_*$  and length/time units are rescaled by  $\mu$ . The dimensional deformation

<sup>2</sup> In this paper, we are not attempting to address concepts such as the formal definition of spherical symmetry in non-integer dimensions, neither the consequences of including fractional derivative operators [33].

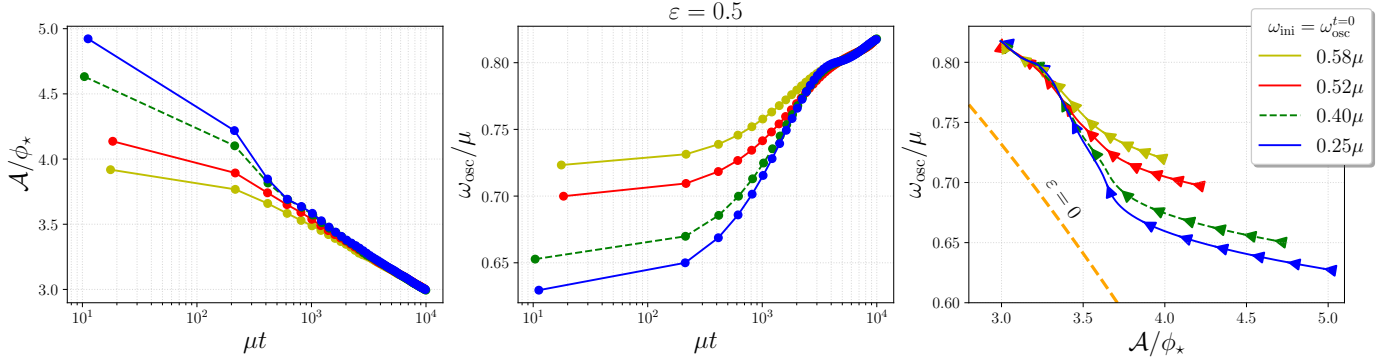


FIG. 2. Parameter flow at  $\varepsilon = 0.5$  for four initial breather frequencies. In the first two panels, we show the evolution of  $\mathcal{A}$  (i.e., the red envelope in Fig. 1) and the oscillon's frequency  $\omega_{\text{osc}}$  as functions of time. We observe that both parameters evolve very quickly towards an attractor. Once the convergence occurs, the flows slow down but do not stop. In the last panel, we see that the flow in parameter space collapses into a line, aligned along the breather flow line (in orange, dubbed as  $\varepsilon = 0$ ) given by Eq. (14). The arrows only represent the direction of time, since the speed can be inferred from the first two panels of this figure.

(proportional to the first radial derivative) can be equivalently treated as a modification in the potential term by a variable redefinition  $u \equiv \bar{r}^{\varepsilon/2} \bar{\Phi}$ . We can estimate the asymptotic solution by replacing the ansatz

$$\bar{\Phi}(\bar{r}) = \sum_{n=1}^N \bar{\Phi}_n(\bar{r}) \cos(\omega t), \quad (12)$$

in Eqns. (9) and (10), yielding,

$$\bar{\Phi}_n(\bar{r}) \sim \bar{r}^{-\varepsilon/2} \exp\left(-\bar{r}\sqrt{1-\omega^2}\right), \quad (13)$$

here  $\omega$  is essentially the Fourier transform of the solution in the time domain. Such a frequency generates freely propagating spherical waves for  $\omega > 1$ , and localized solutions otherwise. In the case of localized states (such as stable oscillons), the exponential decay dominates over the fractional power and also gives a crude estimate of the objects' size. Nevertheless, it is crucial to filter the scattering states as the solution evolves, since fractional power law decays may affect the convergence of the numerical routine. In Appendix A, we explain in detail how to configure the pseudospectral numerical routine used to produce spherically symmetric oscillons in  $D = \varepsilon + 1$  dimensions.

In Section V, we will introduce another way to modify the sine-Gordon equation correcting the potential and representing the dynamical state of the solutions by considering the same parameters described in this section. Some of the results in the ( $\varepsilon < 1$ ) regime of dimensional deformations will also extend to corrections in the curvature of the field's potential. It is important to notice that, for most of this paper, the dimensional parameter  $\varepsilon$  is kept a constant in time. It is only in Sec. VI where we introduce new time-dependent deforming operators from the Lagrangian to control the speed of the dimensional transitions.

## B. Anatomy of the deformed solutions and diagnostic parameters

Solving the SG model modified by a dimensional deformation in (9, 10) allows us introduce the radial structure of the oscillon core and its evolution. In the first two panels of Fig. 1, we show the evolution of two solutions using different initial conditions: one which is stable, and another decaying after (approx.) a hundred oscillations. Considering  $\varepsilon = 0.75$ , both panels are consistent with the generation of an oscillons since the oscillating fields are spatially localized. The left panel shows just a few oscillations of a long-lived solution. A closer look at this panel reveals small dissipative effects (minor changes in the shape and tails) associated to the emission of classical radiation, which propagate energy outwards. The middle panel depicts the decay process of an oscillon, showing how the amplitude reduces, the frequency increases and the solution becomes broader.

Knowing that the breather's oscillation frequency  $\omega_{\text{ini}}$  is the only parameter required to set initial conditions, it is reasonable to measure the frequency of the solutions of Eqns. (9, 10) (from now on, dubbed as  $\omega_{\text{osc}}$ ) to learn about the dynamical state of the deformation. In the right panel of Fig. 1, we trace the oscillation of the solution at  $r = 0$ . The panel at the top shows that the evolution of the amplitude envelope (in red) becomes slower after a few ( $\sim 10$ ) oscillations, but it does not stop. With this envelope, it is possible to consider the solution amplitude  $\mathcal{A}$  at the origin as an auxiliary time-dependent parameter. In the lower panel, we plot the power spectrum of the field evolution at the center. Such a spectrum is peaked at several frequencies, from which the highest of all peaks is at  $\omega = \omega_{\text{osc}}$ . An advantage of computing diagnostic parameters from the power spectrum is that if the solutions have converged, it is less prone to be sensitive to the specific details of a numerical implementation. This is in agreement with the argument of multiple frequencies

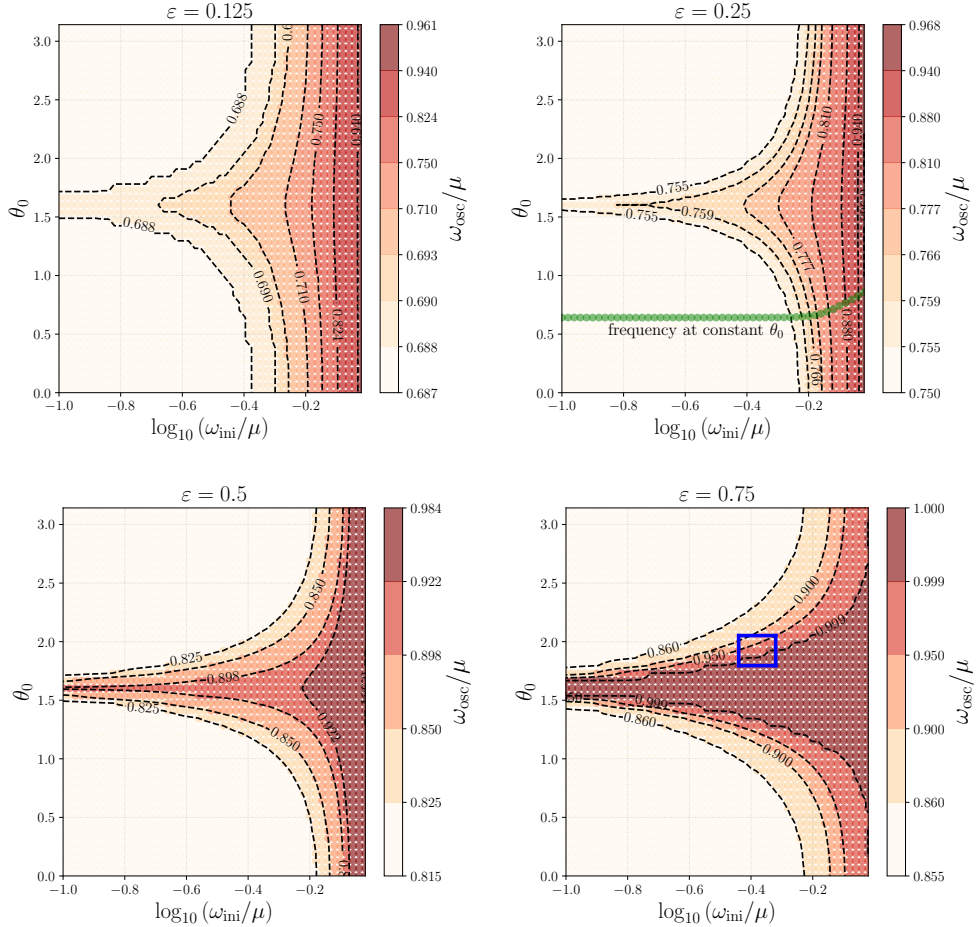


FIG. 3. Frequency of the oscillon as a function of the phase and frequency of the initial SG breathers for  $\varepsilon = 0.125, 0.25, 0.5$  and  $0.75$ . The frequency of stable oscillons (colored in yellow in all of the panels) formed by wide and squared breathers increases with  $\varepsilon$ . As expected, the quantity of scenarios where stable oscillons (with  $\omega_{\text{osc}} < \mu$ ) are formed tends to decrease as  $\varepsilon$  increases. Throughout the remaining sections of this paper, the dependence of the oscillation frequency in  $\omega_{\text{ini}}$  (visible in the constant phase green curve at  $\varepsilon = 0.5$ ) will be transformed into a function of energy to represent the dynamical state of the oscillating field. Solutions within the red regions may have non-trivial modulation in their core during the transient. The cases enclosed in the blue rectangle ( $\varepsilon = 0.75$ , in the right bottom panel) exhibit time-dependent modulation in their amplitude, which will also be observed in the non-perturbative regime.

coexisting in the solution, as stated in [17]. Strictly speaking, flowing parameters are time-dependent quantities; nonetheless, after the initial transient the solution hits an attractor the flow is sufficiently slow to consider negligible time derivatives. To corroborate that, we evaluate the frequency and amplitude as functions of time given four initial breathers. The time-dependence of  $\omega_{\text{osc}}$  is determined by separating the solutions of  $\phi(0, t)/\phi_{\star}$  in a number of bins, as in a spectrogram. Thus, we can extract the dominant frequency and the lower time bound in each bin. As for the amplitude  $\mathcal{A}$ , we used the routine `find_peaks` in `scipy.signal` [34] to find the peaks and the instants of time when these occur. Field amplitude envelopes are built by interpolating some subsets of the amplitude maxima; to do so, one may use interpolating univariate splines (IUS) in `Scipy`, for example. As a result of this, we show in Fig 2 the convergence of the parame-

ter flows to form an attractor in the  $(\mathcal{A}, \omega_{\text{osc}})$  projection. When  $\varepsilon = 0$ , the breather solution yields the amplitude as a function of the oscillation frequency

$$\mathcal{A}_{\text{br}} = 4 \tan^{-1} \left( \frac{\sqrt{1 - \omega_{\text{ini}}^2}}{\omega_{\text{ini}}} \right). \quad (14)$$

which corresponds to the unperturbed case plotted in an orange dashed line in the rightmost panel. Interestingly, the attractor is (approximately) aligned with the baseline flow. From the left and middle panels, we observe that the time needed to converge is small compared to the time flowing along the attractor. The formation of attractors is consistent with many preexisting results for oscillons in  $D \leq 2$  spatial dimensions, such as in [21, 22], even when our manuscript does not consider mutually interacting solutions.

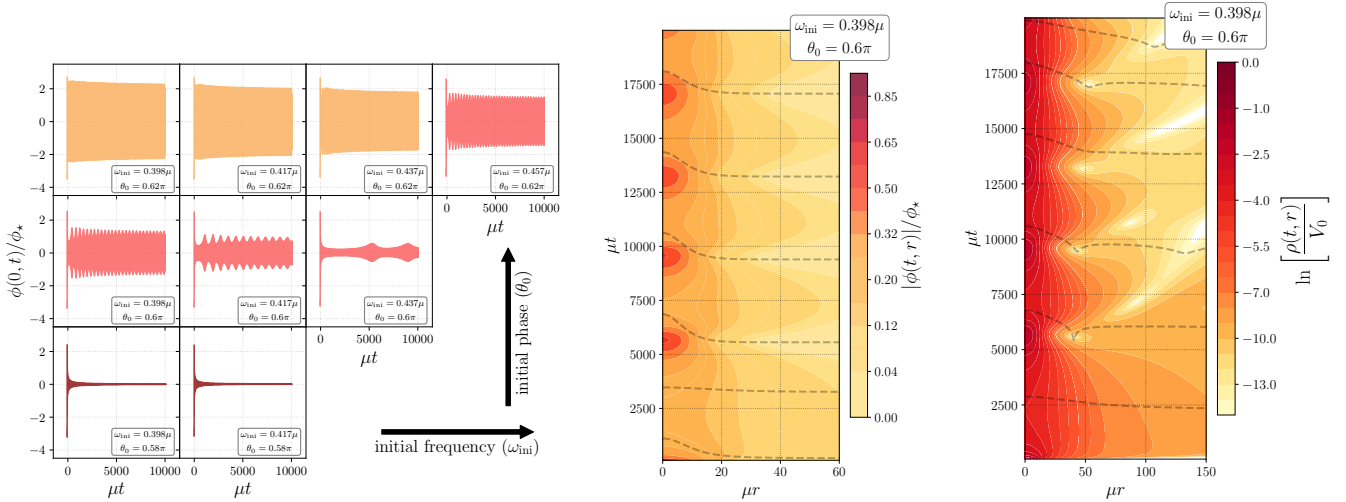


FIG. 4. Left panel: Time evolution of  $\phi(0, t)/\phi_*$  for some of the solutions in the blue rectangle (case  $\varepsilon = 0.75$  of Fig. 3). We are using the same color code as in the previous figure, showing that the solutions with modulated amplitude serve as “transition solutions” between the stable oscillons (in orange) and the fast decaying profiles (in brown). Interestingly, the frequency of the modulating envelope reduces as one approaches the short-lived solutions. Central panel: Spatial structure of an amplitude modulated for  $\varepsilon = 0.75$ . Amplitude modulation corresponds to an intermittent contraction and expansion of the oscillon core. Right panel: Energy density as a function of radius and time for the solution in the middle panel. Modulation occurs as energy leaves the core in a discrete number of bursts. Smooth black dashed lines correspond to constant-time snapshots of the field and its energy density, rescaled to fit in the panel.

The energy of the oscillating field is another parameter useful to assess the dynamical state of the initial breathers as these deform. Due to the emission of classical radiation bursts throughout the whole evolution of the field (which is more intense during the initial transient phase), the solution’s energy is a time-dependent quantity. In this setup is given by

$$\rho(r, t) = \frac{1}{2} \left( \frac{\partial \bar{\Phi}}{\partial t} \right)^2 + \frac{1}{2} \left( \frac{\partial \bar{\Phi}}{\partial r} \right)^2 + (1 - \cos \bar{\Phi}), \quad (15)$$

$$\frac{E}{\mu^{\varepsilon+1} V_0} = \frac{2\pi^{\frac{\varepsilon+1}{2}}}{\Gamma\left[\frac{\varepsilon+1}{2}\right]} \int_0^{R_{\max}} dr r^\varepsilon \rho(r, t), \quad (16)$$

where, for conciseness, we omit the bars on top of  $r$  and  $t$ ; and the upper limit  $R_{\max}$  is the total size of the simulation box, which is set to infinity.  $E_{\text{init}}$  denotes the energy of the spherically symmetric initial breather as reported in Eqns. (6–8), which depend on the initial phase  $\theta_0$ . For  $t = 0$ ,  $\theta_0 = \pi/2$  cancels the potential energy contribution, and  $\theta_0 = 0$  sets the time-derivative to zero, suppressing the kinetic energy. It is important to clarify that the initial configuration has a radial profile identical to an SG breather (except in Sec. IV), but its energy is given by the integral in (16) for all the cases with  $\varepsilon$  strictly greater than zero. Hence, the initial state energy is not the same as for one-dimensional objects, with the exception of the analysis in Section V. Absorbing boundary conditions are placed to exponentially suppress the classical radiation emitted during the transient phase in less than a few hundred oscillations, and are located as close to the oscillon core as they can. Hence the integral

in (16) is a good approximation of the energy stored in the oscillon after a thousand oscillations or so.

### III. DIMENSIONAL DEFORMATIONS IN THE PERTURBATIVE REGIME

In this section, we evaluate the connection between SG breathers with the oscillons generated after solving Eqns. (9) and (10) in the case where the dimensional correction is as small as it can be (i.e., when  $\varepsilon < 1$ ). We realize this connection via the oscillon frequency  $\omega_{\text{osc}}$ , which is treated as a control parameter defined and measured as indicated in the right panel of Fig. 1. Parameter evolution in the first two panels of Fig. 2 show that the convergence to an attractor basin lasts slightly longer than the transient phase. After that, it is reasonable to treat  $\omega_{\text{osc}}$  as a slowly varying parameter obtained from the numerical solutions of Eqns. (9) and (10). We bin the oscillation frequencies and plot color coded contours in Fig. 3 for different breather-like initial conditions, which are labeled by their frequencies  $\omega_{\text{ini}}$  and phase  $\theta_0$ . The frequency is extracted from the field solution evaluated at the origin until  $t = 10^4 \mu^{-1}$ , allowing a few thousand oscillations of evolution. Red and brown contours in the lower frequency regime ( $\log_{10}(\omega_{\text{ini}}/\mu) \lesssim -0.3$ ), in all of these panels reveal some preference to form lower frequency oscillons when the initial breathers have more potential than kinetic energy. In the two upper panels (corresponding to  $\varepsilon = 0.125$  and  $0.25$ ), this is less noticeable since the contours do not represent large frequency variations.

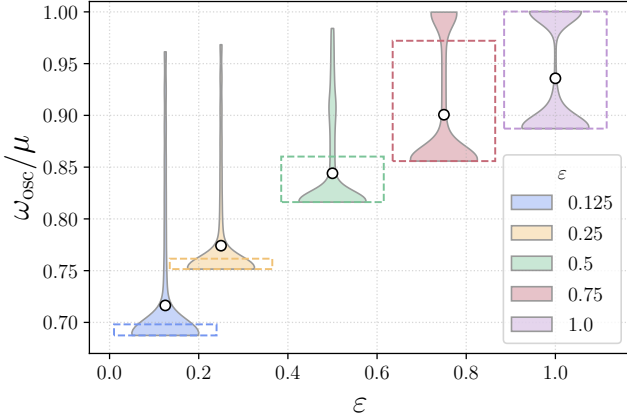


FIG. 5. After counting the number of solutions in each panel of Fig. 3, we find the deformation of the probability distribution functions as a function of  $\varepsilon$ . The rectangles contain 75% of the distributions' mass, showing that at  $\varepsilon = 1$  the remaining 25% of the samples do not form stable oscillons. The dots represent the mean frequency of the sample displacing upwards as  $\varepsilon$  increases.

The formation of attractors in parameter space (as depicted in Fig. 2) is a foreseeable feature, visible in all the panels of Fig. 3, particularly in the ivory regions denoting the degeneracy of nearly squared breathers with different initial frequencies to form the same oscillons. Constant frequency contours look like straight vertical lines near  $\omega_{\text{ini}}/\mu \sim 1$ , which is the usual regime where solutions only oscillate around the potential basin centered at  $\phi = 0$ . Contour deformations (producing the spikes centered at  $\pi/2$  in Fig. 3) appear when the solution spills over more than one potential well, entering in the regime of wide and squared initial breathers. In this regime, the energy density profile bounces toward the origin and energy localization is not clear. Fast-decaying solutions start to emerge as  $\varepsilon \rightarrow 1$ , this can be noticed in the upper frequency limit of the color bars since  $\omega_{\text{osc}}^{\text{max}} \rightarrow 1$  as  $\varepsilon \rightarrow 1$ .

Let us zoom in the features of the rectangular patch in blue, visible in the panel labeled as  $\varepsilon = 0.75$  in Fig. 3. In the left panel of Fig. 4 we select a few solutions evaluated at the center  $r = 0$ , noticing the existence of amplitude modulated oscillons in the region separating stable (in ivory) from unstable (in brown) solutions. This suggests that the region in red serves as a transition zone between stable and unstable solutions, showing that amplitude modulations are dynamical features of the solution. Strictly speaking, the modulation is not limited to the solutions colored in red in Fig 3 and the left panel of Fig 4. It extends through the range of initial frequencies ( $\omega_{\text{ini}}$ ) in a way that the time interval between intermittent oscillations decreases (up to the point of being negligible) as the frequency of the initial breather reduces. As  $\omega_{\text{ini}}$  increases, the modulated envelope reaches its lowest frequency before finding an unstable solution. In the middle panel of the same figure, we observe the spatial properties of the modulated solution by plotting  $|\phi(r, t)|/\phi_{\star}$ , noticing

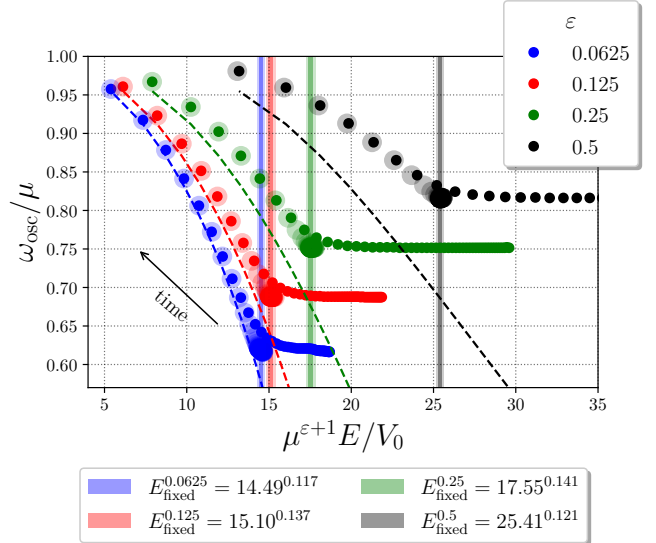


FIG. 6. Oscillation frequency ( $\omega_{\text{osc}}$ ) as a function of the initial energy (solid dots) and the energy after a few hundred oscillations (transparent dots). Vertical colored lines indicate the energy ( $E_{\text{fixed}}$ , reported in the legend below), where solutions from large initial breathers cluster. Dashed lines represent the range of  $\omega_{\text{ini}}$  as a function of the initial energy. Convergence of the dotted and dashed lines indicates the range where oscillons are well-approximated by sine-Gordon breathers.

ing that the amplitude modulation is a consequence of the contraction and expansion of the oscillon core. In the right panel, we plotted the radial structure of the evolving energy density for the same oscillon described in the middle panel. Intermittency occurs due to the emission of classical radiation in discrete bursts propagating outside the oscillon's core. Classical radiation propagates outside the simulation box at (approximately) the speed of light. Solutions showing intermittent periods of contraction and expansion also appear in two (and more) spatial dimensions, these will be discussed in Sec. IV. An important fact to remark is that these solutions (similar to the asymptotic ansatz used in Eq. (12)) are not consistent with the quasibreather prescription

$$\frac{\phi(r, t)}{\phi_{\star}} = \sum_{n \in \mathbb{N}} R_n(r, \omega) \sin(n\omega t + \delta_n), \quad (17)$$

which is given in multiples of the “fundamental frequency”  $\omega$ , as stated in [4, 17]. The spatial structure visible in the middle and right panels of Fig 4 reveal that these solutions are still spatially localized. We suspect (but still cannot confirm) that these solutions are related to the emission of staccato radiation in oscillons [19, 20].

Each of the panels in Fig. 3 measured the oscillation frequency of 2500 oscillons starting from initial conditions within the frequency range of  $(-1.0 \leq \log_{10}(\omega_{\text{ini}}/\mu) < 0.0)$  for  $\omega_{\text{ini}}$ , and  $(0.0 \leq \theta_0 < \pi)$  for the phase. Such intervals contain 50 points each. Thus, we have sufficient simulations to find how the frequency distributions change as

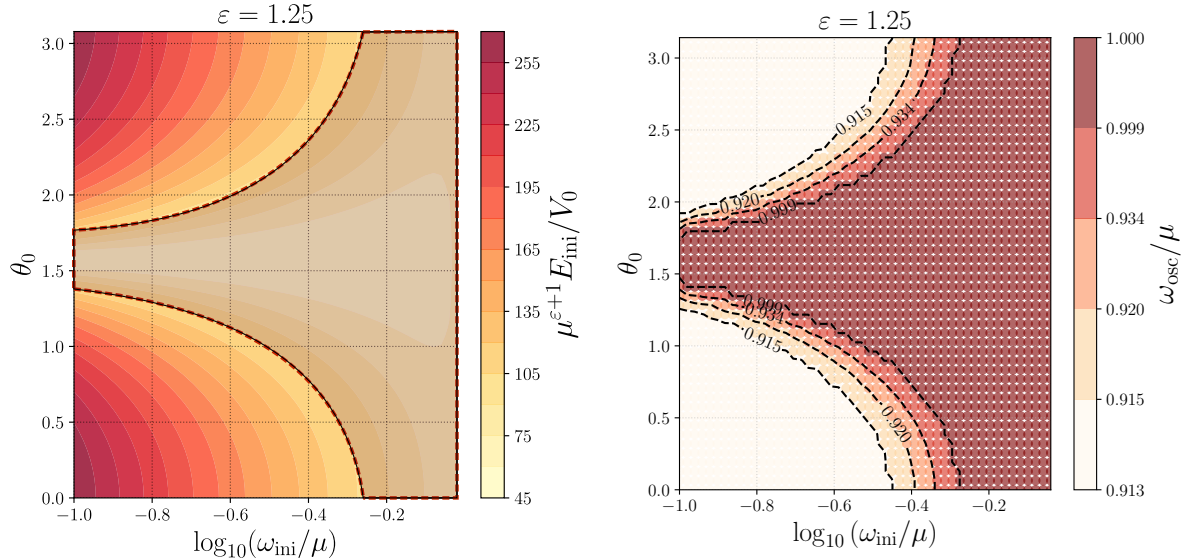


FIG. 7. Initial energy (left panel) and oscillation frequency  $\omega_{\text{osc}}$  (right panel) as functions of the initial breather parameters for  $\varepsilon = 1.25$ . Parameterizing initial conditions with SG breathers discards a non-trivial fraction of the accessible states (inside the red/brown contours in the right panel, and in the shaded region in the left panel). Showing that in the non-perturbative limit, breathers may not have sufficient energy to produce stable solutions.

the dimensional deformations of the SG equation become more significant (i.e., as  $\varepsilon$  grows). In Fig. 5, we used `violinplot` in `Matplotlib` [35] to show that the  $\omega_{\text{osc}}$  distribution functions deform progressively from being unimodal ( $\varepsilon \ll 1$ ) to be bimodal ( $\varepsilon \sim 1$ ), and the range of oscillation frequencies contracts and shifts toward larger frequencies as  $\varepsilon$  grows. For  $\varepsilon = 0.5$ , the distribution plotted in green clearly represents an intermediate stage between the unimodal ( $\varepsilon = 0.125$  and  $0.25$ ), and the bimodal distributions ( $\varepsilon = 0.75$  and  $1.0$ ). The interval shift is also visible from the displacement of the ensemble's mean, this is depicted by the white dot of each distribution. An important body of work including analytical results, argues that there are no theoretical constraints on the formation of small-amplitude oscillons for  $\varepsilon \leq 1$  (e.g., [36–38]). We must remark that the purpose of this figure is only to visualize deformations in the frequency range and in the availability of oscillons given a finite span of initial conditions, without spanning an infinite energy span. However, our findings do not show evidence of a low-amplitude minimum. For  $\varepsilon = 0.125$  and  $0.25$ , the long tails in the distribution functions still contain a non-trivial fraction of the states. As  $\varepsilon$  increases, our results in Fig. 5 suggest that most of the solutions in the tails eventually accumulate in  $\omega_{\text{osc}}/\mu \sim 1$ , which means these have decayed. Nevertheless, some of them remain in the thin filaments separating the decayed and stable regimes in the distributions. Those configurations correspond to oscillons showing intermittent phases of contraction and expansion of their cores.

The green dotted curve containing constant phase simulations in the  $\varepsilon = 0.5$  panel of Fig. 3 represents the dependence of the oscillation frequency ( $\omega_{\text{osc}}$ ) on the ini-

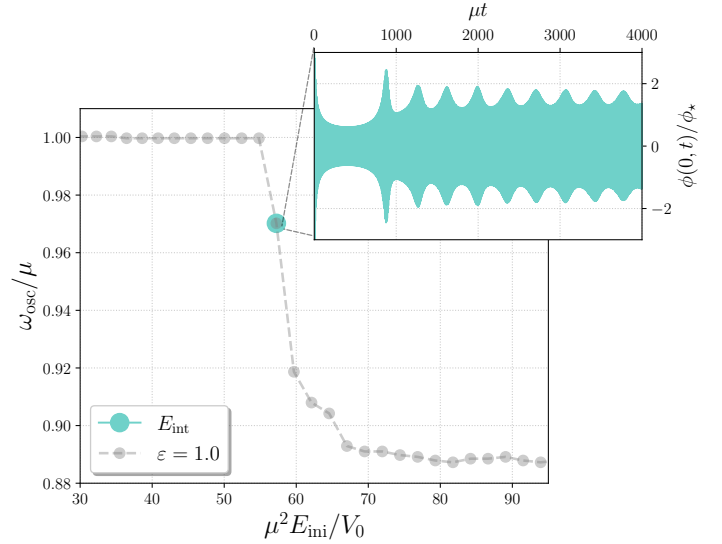


FIG. 8. The diagnostic parameter  $\omega_{\text{osc}}$  as a function of the initial energy  $E_{\text{ini}}$  in 2D. The amplitude modulated solution is an intermediate state between decayed and stable solutions.  $E_{\text{int}}$  is the initial energy necessary to produce the amplitude modulated field.

tial breather frequency. Such a dependence will be studied and reparameterized in what remains of this paper, considering also how does it vary with the dimensionality and with other forms of model deformations (see Sec. V). Showing that different elements of the map contain important information about the dynamical state and the availability of oscillons. In Fig. 6, we set the initial phase

to zero to show the dependence of  $\omega_{\text{osc}}$  with the initial energy in solid color dots. Constant frequency plateaus (to the right of the big dots) represent the solutions plotted in ivory in Fig. 3, produced by breathers in the collapsing shell regime, which have initial frequencies in the order of  $0.1\mu$ . The smooth low-energy incline is consistent with the existence of infinitely many oscillons with arbitrarily small energy, as reported in [36–38]. Large semi-transparent dots represent the relation between the oscillation frequency and energy after a few hundred oscillations. Here we also notice that the points in the initial energy plateaus collapsed to a large colored blob, representing the same solution.  $E_{\text{fixed}}$  is the energy of the solution collapsed to a single colored blob, and reported in the lower legend. We notice that both the energy and the oscillation frequency keep decreasing as  $\varepsilon \rightarrow 0$ . Initial breather frequency  $\omega_{\text{ini}}$  is plotted in dashed lines as a function of the initial energy (computed from Eq. (16)). When  $\varepsilon < 1$ , lines dotted in solid and semi-transparent colors concur as  $\varepsilon \rightarrow 0$ , suggesting that sine-Gordon breathers are decent approximations of the oscillon for energies below  $E_{\text{fixed}}$ . From the same figure, regions where such a convergence occurs can be found in the smooth incline at the low-energy regime.

As oscillons evolve, they lose energy in the form of classical radiation, becoming wider as their amplitude and oscillation period reduce. Thus, the state labeled by the “blob” in black moves upwards as it goes to the left, following the trajectories marked with dots in the direction of the black time arrow. Contraction of the oscillation frequency range becomes evident as  $\varepsilon$  increases, which is consistent with the distributions in Fig. 5. Uncertainties reported in the legend are found from the variance of the state accumulation that collapsed to a single point around  $E_{\text{fixed}}$ . The slopes of the low-energy inclines seem to reduce as the number of spatial dimensions grow, going to zero in the non-perturbative regime, as will be shown in Sec. IV. In that section, it is also possible to notice that the original breather parameterization of initial conditions induces a severe reduction in the number of available oscillons, for  $D \geq 2$  spatial dimensions. In Section V, we extend our analysis to treat potential deformations of breather solutions still yielding oscillons in one spatial dimension.

#### IV. DEFORMATIONS BEYOND THE PERTURBATIVE REGIME

In this section, we extend our analysis for oscillons in  $D \geq 2$  spatial dimensions. Nevertheless, it is not possible to use the same parameterization of initial conditions as in the perturbative regime, as developed in Sec. III. In Fig. 7, for  $\varepsilon = 1.25$ , we show that the energy budget from SG initial breathers severely restricts the number of accessible states. The shaded region in the left panel overlaps with the regions colored with red/brown dots in the right panel, representing a large fraction of the initial

parameter space without stable solutions. Moreover, the evolution of initial breathers with  $\omega_{\text{ini}} \gtrsim 0.6\mu$  does not produce solutions with significant amplitudes. Energy is quickly radiated away for initial states oscillating around a single potential well centered at  $\phi = 0$ . Such a restriction becomes even more stringent for larger values of  $\varepsilon$ . A simple way to inject more energy into the system is to introduce an extra parameter  $\alpha$ , such that

$$\frac{\phi(r, t)}{\phi_*} = 4\alpha \tan^{-1} \left[ \frac{\sqrt{1 - \omega_{\text{ini}}^2} \cos(\omega_{\text{ini}} t - \theta_0)}{\omega_{\text{ini}} \cosh(\sqrt{1 - \omega_{\text{ini}}^2} r)} \right], \quad (18)$$

introduces both kinetic and potential energy for  $\alpha > 1$ . The extra energy budget can be used to produce both bound and scattering states. Our primary objective is to describe the oscillation frequency flow and connect it to oscillon (i.e., bound states) dynamics in energy scales where the transitions from stable to fast-decaying oscillons occur. For this purpose, we sample energies by following the flow line of initial parameters

$$\alpha = -2 \log_{10} \left( \frac{\omega_{\text{ini}}}{\mu} \right), \quad (19)$$

in the initial frequency range  $\log_{10}(\omega_{\text{ini}}/\mu) \in [-1.0; -0.2]$ , which crosses transversally the constant initial energy level curves for solutions in two or three spatial dimensions. Distortions in the initial frequency range result in amplitudes shifted by, at most, a factor of two. Injected energy is not enough to generate abundant stable states; nonetheless this frequency/amplitude range is sufficient to study solutions around the transition energy. Even when a careful analysis of lifetimes is not in the scope of this paper, we find (as expected) that the lifespan of two-dimensional oscillons is several orders of magnitude larger than in 3D, where solutions oscillate for a few hundred oscillations at most. To be fully consistent with the analysis in previous section, we also consider  $\omega_{\text{osc}}$  (defined as the dominant oscillation frequency of the solution at  $r = 0$  up to  $t = 10^4\mu^{-1}$ , as detailed in Fig. 1) as a control parameter used to determine the dynamical state of the system. For stable oscillons following the parameter flow line in (19) in  $D < 2$  spatial dimensions, the shape and evolution of radial profiles for stable, unstable and amplitude modulated solutions is consistent with the results we presented in the previous section. After using the initial conditions stated in (18), its time derivative for  $\theta_0 = 0$ , and the parameter flow line from Eq. (19), we plot in Fig. 8 the dependence of the control parameter  $\omega_{\text{osc}}$  on the initial energy  $E_{\text{ini}}$  for  $\varepsilon = 1.0$  (i.e., spherically symmetric oscillons in 2D). We find an oscillon with quasi-periodic amplitude modulation sitting in the intermediate region between stable and rapidly-decaying field configurations, which is similar to our results reported in the bottom right panel of Fig. 3 for  $\varepsilon = 0.75$ . If we consider the set of solutions as a two-state system (which is also noticeable in the maps in Fig. 3), made out of stable and unstable solutions. This confirms our intuition that

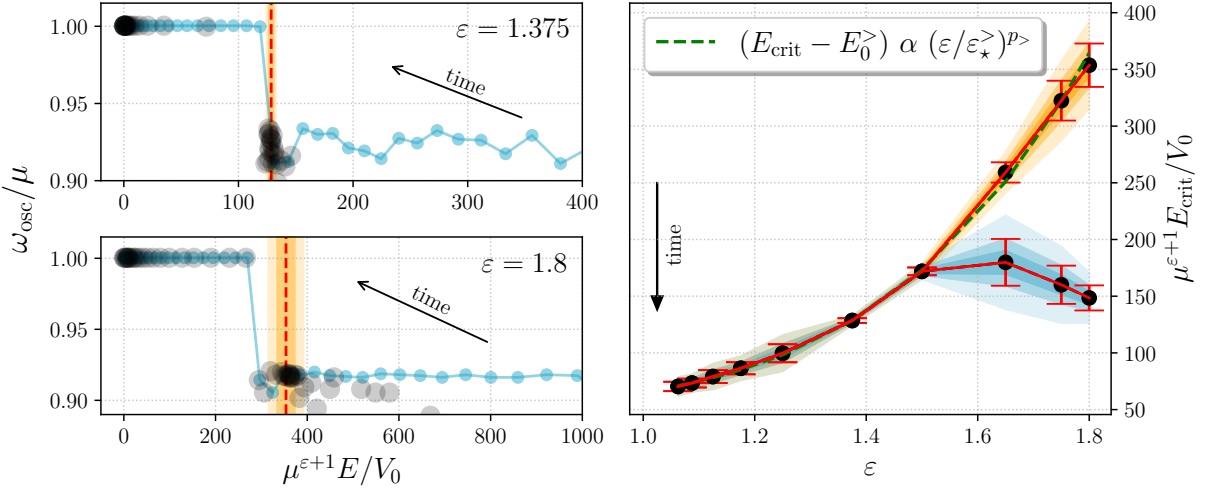


FIG. 9. Left panels: Oscillation frequency as a function of the initial energy (small blue dots) and the energy after a few hundred oscillations at  $t = 3 \times 10^3 \mu^{-1}$  (large semi-transparent black dots) for  $\varepsilon = 1.375$  (upper figure) and  $\varepsilon = 1.8$  (lower figure). From the two figures, it is clear that the two clusters of black points denote states that at low energies (and  $\omega_{\text{osc}} \sim \mu$ ) have already decayed. At higher energies, marked by the red dashed lines for frequencies  $\omega_{\text{osc}} < \mu$ , the clustered points correspond to the same stable oscillons. Right panel: Dots colored in solid black are the stable solution energies (indicated by red dashed lines in the left panels) where the stable states accumulate, rendering (approximately) a monotonically growing function of  $\varepsilon$ . As time progresses, the solutions in  $D \lesssim 3$  dimensions are the first to move away from the power law, as shown in the collection of points shaded in blue.

amplitude modulation is the way describe the dynamics in the transition zone.

As mentioned in the previous sections, the energy in the simulation box is an important parameter to determine the dynamical state of the solution. An important role of the energy (measured at different times) is to discern which initial configurations yield the same final state, as we observed in the perturbative regime in Fig. 6; and whether the initial energy budget is sufficient to produce stable oscillons or not. Therefore, the message contained by the green constant phase curve (at  $\varepsilon = 0.5$ , in the upper right panel) in Fig. 3 can be extended further into the  $\varepsilon > 1$  regime. Following the initial conditions determined by the parameter flow line in Eq. 19, the blue dots in the left panel of Fig. 9 show how the frequency  $\omega_{\text{osc}}$  depends on the initial energy, in the same way as in Fig. 8. Large semi-transparent black dots illustrate the relation between the same frequency and the energy after a few hundred oscillations for  $\varepsilon = 1.375$  and  $\varepsilon = 1.8$ . In both cases, it is possible to distinguish two states: rapidly-decaying solutions with low energies, and stable solutions with larger energies and  $\omega_{\text{osc}} < \mu$ . States accumulate to form the “blobs” shaded in black, since (a) attractors in functional space cluster states with sufficient energy, as discussed in Sections II, III, and in many other places in the literature [21–23]. In addition to this, (b) every solution (stable or unstable) eventually decays. In both figures, the number of states in the low initial energy plateau is the same as in the accumulation of black points with  $\omega_{\text{osc}} \sim \mu$ . As time progresses, oscillons lose energy and increase their oscillation frequency, moving upwards

directly (along the black arrow) to the clusters of decayed solutions in the upper left corner of the plots.

Apart from the existence of intermittent core modulations, this is another instance where the language of critical behavior is relevant in our discussions: in contrast to what happens in the perturbative regime, the absence of intermediate points in the transit from the cluster of stable states suggests the presence of a phase transition for  $\varepsilon \geq 1$  (i.e., in  $D \geq 2$  spatial dimensions). The transition from stable to unstable oscillons is also visible in the abruptness of the frequency “jump” in the curves plotted in light blue, which means that this can be diagnosed by computing the energy of the initial solutions. There is an interesting connection with our results from the perturbative regime in Fig. 6: as  $\varepsilon$  grows, the low-energy band becomes less populated with stable oscillon states, transitioning to form one rapidly decaying solution as the slope of the smooth incline (as seen in the perturbative regime) goes to zero. The presence of intermediate amplitude modulated oscillons happens at the energy transitions, and requires more frequency/energy resolution to detect such states as  $\varepsilon$  grows. In our simulations, we find that the low initial energy plateau of unstable solutions becomes visible at  $\varepsilon \sim 1$  (in our set of simulations, this was evident at  $\varepsilon = 0.75$ ).

Considering the energy values where stable oscillons can be safely found, we measured it for several values of  $\varepsilon \in (1.0; 2.0)$  to plot, in the right panel of Fig. 9, the critical energy as a function of the number of spatial dimensions. The fact that points cluster around a specific value introduces a fuzziness parameter as variance (in

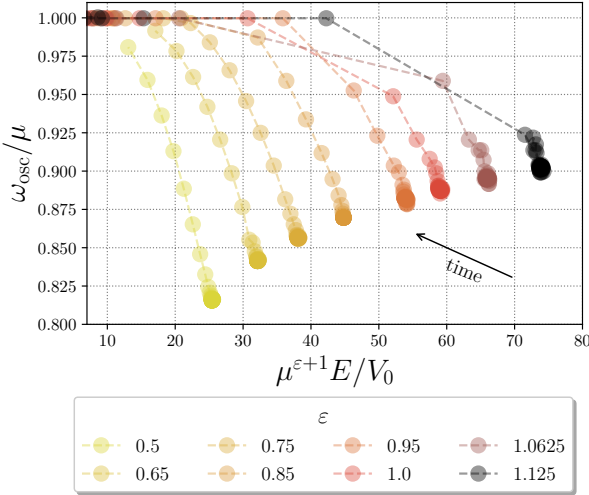


FIG. 10. Contraction of the oscillation frequency range in the transition from the perturbative to the non-perturbative regime of breather deformations. Intermediate frequency configurations become harder to find as  $\varepsilon$  increases. Decayed states with  $\omega_{\text{osc}} = \mu$  appear at  $\varepsilon = 0.75$ .

both frequency and energy) – also represented in the left panels as the orange regions around the vertical lines dashed in red – which is included as the red error bars plotted in this panel. Due to the shorter lifespan of the solution, it is difficult to identify the oscillon with a single frequency, hence the size of the error bars becomes larger as  $\varepsilon \rightarrow 2$ . Regions shaded in different tones of orange contain one, two and three sigma areas containing the central curve (in red). Regardless of the error bars size, it is clear that the critical energy grows as the dimensionality increases. With the emission of classical radiation, more solutions leave the stability region to dilute, implying that eventually the monotonically growing curve flattens to zero. We used `curve_fit` in `SciPy` [34] to produce an error-weighted fit, showing in the curve dashed in green that the critical energy can be approximated by a power law proportional to  $\varepsilon^{p_>}$ , with  $p_> = 5.15 \pm 0.15$ , with no intercept in the energy axis. The power of  $\varepsilon$  has a tendency to grow slightly if we exclude from the fit the points with largest errors. A naive extrapolation to the limit  $\varepsilon \rightarrow 0$  will obviously cancel the critical energy. Energy and oscillation frequency are not reliable parameters for oscillons in  $D \lesssim 3$  using the timescales considered in the perturbative regime. In such cases, oscillons have shorter lifetimes and therefore, average diagnostic parameters depend on rapidly changing solutions.

The features due to perturbative ( $\varepsilon < 1$ ) and non-perturbative ( $\varepsilon > 1$ ) dimensional deformations become clearer in Fig. 10. Here we show how the solutions are distributed for different values of  $\varepsilon$  starting from a uniform distribution of SG breathers. For  $\varepsilon = 0.65$ , none of the solutions has decayed; nonetheless, for  $t = 10^4 \mu^{-1}$  and  $\varepsilon = 0.75$  it is possible to see the first decayed configurations. There is a maximum energy where solutions

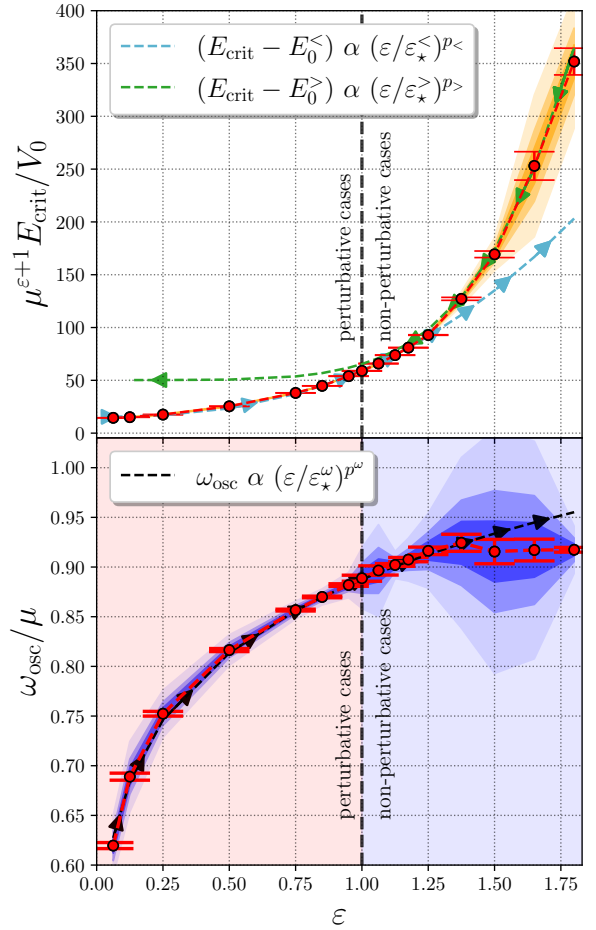


FIG. 11. Energy (upper panel) and oscillation frequency (lower panel) of oscillons generated by low-frequency breathers as a function of the number of spatial dimensions. The notion of minimal energy to form an oscillon does not apply to the perturbative regime, since this is an upper energy bound representing the oscillons produced by low-frequency (wide and squared) initial conditions.

case	$E_0[\mu^{\varepsilon+1}/V_0]$	$\varepsilon_*$	$p$
$(<)$	$15.54 \pm 0.66$	$0.21 \pm 0.01$	$2.47 \pm 0.07$
$(>)$	$50.26 \pm 2.44$	$0.947 \pm 0.001$	$5.15 \pm 0.15$

TABLE I. Fitting coefficients and uncertainties for the perturbative and non-perturbative energy fits presented in Figs. 9 (green curve, right panel) and 11. In the perturbative case, critical energy coincides with the oscillon energy in two dimensions.

remain accumulated, located at one extremum of the frequency span in all of the cases. For  $\varepsilon \leq 1$ , we notice a number of states with intermediate oscillation frequencies, smoothly connecting stable and decayed solutions. Such a smooth transition progressively deforms to the point of becoming an abrupt frequency transition, with almost no states in between. In Fig. 11, we show the energy and

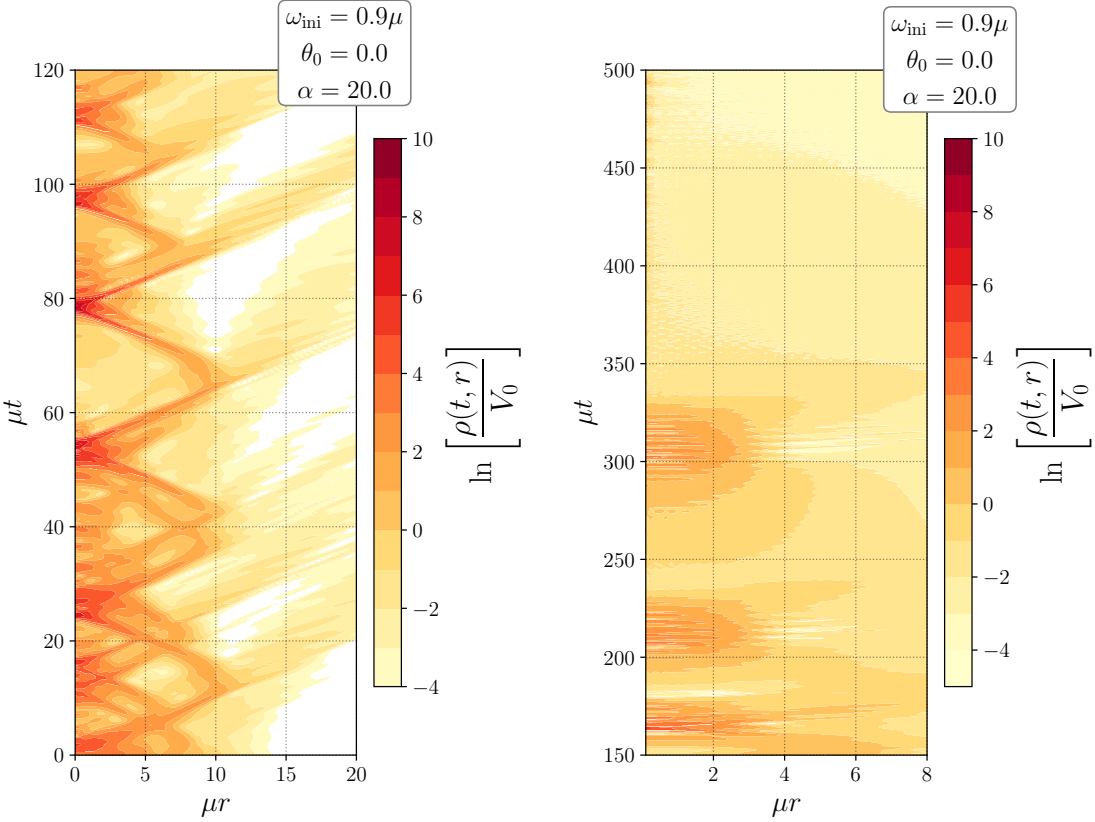


FIG. 12. Evolution of the energy density of a breather-like initial condition in the three-dimensional sine-Gordon model for  $\omega_{\text{ini}} = 0.9\mu$  and  $\alpha = 20$ . When  $\alpha = 1.0$ , the frequency corresponds to a breather oscillating inside the well minimum centered at  $\phi = 0$ . Left panel: Initial phase of the evolution corresponding to the collapse and expansion of spherical shells. Right panel: Dilution of the bound states, the solution disappears after two intermittent bursts.

oscillation frequency as a way to summarize our results for the oscillons produced by collapsing shells. For  $\varepsilon < 1$ , solutions (in the blue region) can be found in the clustered in the upper energy bound (depicted by the large colored blobs in Fig. 6). For  $\varepsilon \geq 1$ , the interpretation changes since non-decayed solutions come from initial conditions behaving as collapsing shells. Therefore, the values of energy in the plot represent the critical energy to form an oscillon from a breather. It is crucial to emphasize that this interpretation does not apply in the cases where  $\varepsilon \ll 1$ . In both panels, we observe that there are no discontinuities in the transition from the perturbative to the non-perturbative regime. We can realize that it is not possible to fit the critical energy as a function of  $\varepsilon$  in a single power law consistent with the data from both the perturbative and the non-perturbative regime. Perturbative and non-perturbative values of the critical energy are represented by separate power laws of the form

$$\frac{\mu^{\varepsilon+1}}{V_0} (E_{\text{crit}} - E_0^{\gtrless}) = \left( \frac{\varepsilon}{\varepsilon_*^{\gtrless}} \right)^{p^{\gtrless}}, \quad (20)$$

where the labels ( $<$ ) and ( $>$ ) refer to the perturbative and the non-perturbative cases from the data, respectively. The green (presented in the right panel of Fig. 9 and in the

upper panel of Fig. 11) and light blue curves correspond to the two power law fits shown in Fig. 11. Table I contains the fitting parameters for both curves, which shows that it is necessary to reset  $E_0$  to be (approx.) the oscilon energy at  $\varepsilon = 1$  if we want to represent the critical energy having a power-law dependence in the number of spatial dimensions. In addition to that, there is a clear mismatch between the power representing the perturbative and the non-perturbative cases, even when there is no visible energy discontinuity in these limits. Such a discontinuity in the power is similar to a phase transition (of order higher than zero) separating the two cases. Energy discontinuities manifest first when  $D \gtrsim 2$  at later times, as we can see in the points surrounded by contours shaded in blue, which are collected at a later instant of time. Empirically, oscillon lifetimes are not sufficiently large to label configurations with energies and frequencies that are approximately time-independent, which enlarges the error bars.

In the case of the oscillation frequency, our results show a non-surprising horizontal asymptote near the limit  $\omega_{\text{osc}} \rightarrow \mu$ , showing no evidence of frequency discontinuities at the transition in  $D = 2$  spatial dimensions. Suggesting that “universality”, as discussed in the study

of critical phenomena [39, 40], may not apply in this case. Error bars have been enlarged by factors of 2.5 and 5 in  $E$  and the oscillation frequency, respectively, to make them visible in the areas shaded in orange (upper panel) and blue (lower panel). As for the task of representing the oscillation frequency as a power law, we find from the data that

$$\omega_{\text{osc}} = \mu \left( \frac{\varepsilon}{\varepsilon_*^\omega} \right)^{p^\omega}, \quad (21)$$

with  $\varepsilon_*^\omega = 2.626 \pm 0.078$  and  $p^\omega = 0.124 \pm 0.003 \sim 1/8$ , the power law prescription does a decent job in fitting the frequency running.

So far, we have explored the transition from stable to rapidly-decaying solutions of the deformed sine-Gordon equation. It is reasonable to ask about the existence of other forms of localized oscillatory solutions given initial conditions with higher energy. To do so, we need to visualize the evolution of the oscillon's radial profile produced by breather-like initial conditions with  $\alpha > 2$ , which is well beyond the initial energy span considered in Figures 9, 10 and 11. Extra energy does not necessarily translate in increasingly stable solutions: there is no guarantee that energy spreads in a way that holds together the kink-antikink bound state. In Fig. 12, we show the radial energy density profile of an initial breather-like solution in three spatial dimensions. Here we consider  $\alpha = 20$ ,  $\omega_{\text{ini}} = 0.9\mu$  and no initial phase as initial parameters. Such a large shift in amplitude sets the breather-like solution way off the potential well centered at  $\phi = 0$ . In the left panel, we observe the collapse and expansion of multiple spherical shells, each of those comes from oscillations around different minima. Bursts of classical radiation escape from the solution throughout its evolution. It is clear that energy is no longer a localized quantity, and the frequency of the solution at the origin may not be a relevant parameter anymore. In the right panel, we see the extinction of the solution: its lifetime is smaller than in the cases of the wide and squared initial breathers with  $\omega_{\text{ini}} \sim 0.1\mu$ . The system does not have sufficient binding energy to hold together a large amplitude breather-like bound state. In 2D, spherical shells are not produced for large initial amplitude deformations and the decay occurs faster. In this particular case, this indicates that most of the exceeding energy is used to produce more scattering than bound states. Concretely, large initial breather amplitudes in  $D \sim 3$  dimensions do not guarantee the formation of long-lived oscillons.

## V. POTENTIAL DEFORMATION OF BREATHERS

The treatment suggested in the previous sections of this paper can be extended to also include the effects of mild potential corrections. To do so, we perturb the one dimensional sine-Gordon breather by correcting the

potential as follows

$$\frac{V(\phi)}{V_0} = \left[ 1 - \cos \left( \frac{\phi}{\phi_*} \right) \right] + \varepsilon_V \frac{\Delta V}{V_0}, \quad (22)$$

$$\Delta V = V_0 \left[ \sqrt{1 + \frac{\phi^2}{\phi_*^2}} + \cos \left( \frac{\phi}{\phi_*} \right) - 2 \right], \quad (23)$$

where  $\Delta V$  contains terms from the axion monodromy potential [25–28]. By the use of this parameterization of the potential modifications, we recover the SG potential when  $\varepsilon_V = 0$  and transform exactly into the axion monodromy potential when  $\varepsilon_V = 1$ . One advantage of defining potential deformations in this way is that it is possible to compute perturbative decay rates in the hierarchies of conserved charges, according to the definitions of quasi-integrability in [29–32]. Initial breather states coincide with the definitions in Eqns. (6), (7) and (8), given by

$$\Psi(x, t) \equiv \frac{\sqrt{1 - \omega_{\text{ini}}^2} \cos(\omega_{\text{ini}} t - \theta_0)}{\omega_{\text{ini}} \cosh(\sqrt{1 - \omega_{\text{ini}}^2} x)}, \quad (24)$$

$$\frac{\phi(x, t)}{\phi_*} = 4 \tan^{-1} \Psi, \quad (25)$$

$$\Pi(x, t) \equiv \frac{\partial \phi}{\partial t}, \quad (26)$$

here we did not consider extra parameters since no form of energy compensation is necessary to improve oscillon stability in one spatial dimension. It is important to mention that initial conditions are chosen to always oscillate around the potential well centered at  $\phi = 0$ , limiting the role of the contributions proportional to  $\varepsilon$  to only represent a mild modification of the potential well curvature. Initial breathers' frequency is in the range  $\omega_{\text{ini}}/\mu \in [0.794; 0.966]$  to “confine” the oscillating solutions in a single potential well centered at  $\phi = 0$ . The equations of motion now describe solutions in one spatial dimension

$$\frac{d\phi}{dt} = \Pi_\phi, \quad (27)$$

$$\frac{d\Pi_\phi}{dt} = \frac{\partial^2 \phi}{\partial x^2} - \frac{V_0}{\phi_*} \sin \left( \frac{\phi}{\phi_*} \right) - \varepsilon_V \Delta V'(\phi), \quad (28)$$

where  $\Delta V'(\phi)$  follows from the potential defined in (23), and for conciseness in the notation we omitted the use of barred units (which absorb the  $V_0$  and  $\phi_*$  dependence) for dimensionless space and time coordinates. We aim to extend our results for the sensitivity of the state availability as functions of  $\varepsilon$  (in Fig. 5) and the energy (in Fig. 6) to deformations in the potential, using the same diagnostic parameters – i.e., the oscillation frequency ( $\omega_{\text{osc}}$ ) and energy – considered for dimensional deformations. As for the oscillation frequency, we evaluate the field at  $x = 0$  and select the dominant frequency from the time series, as described in Fig. 1. Oscillon energy is another parameter describing the dynamic state of the solution. It is given

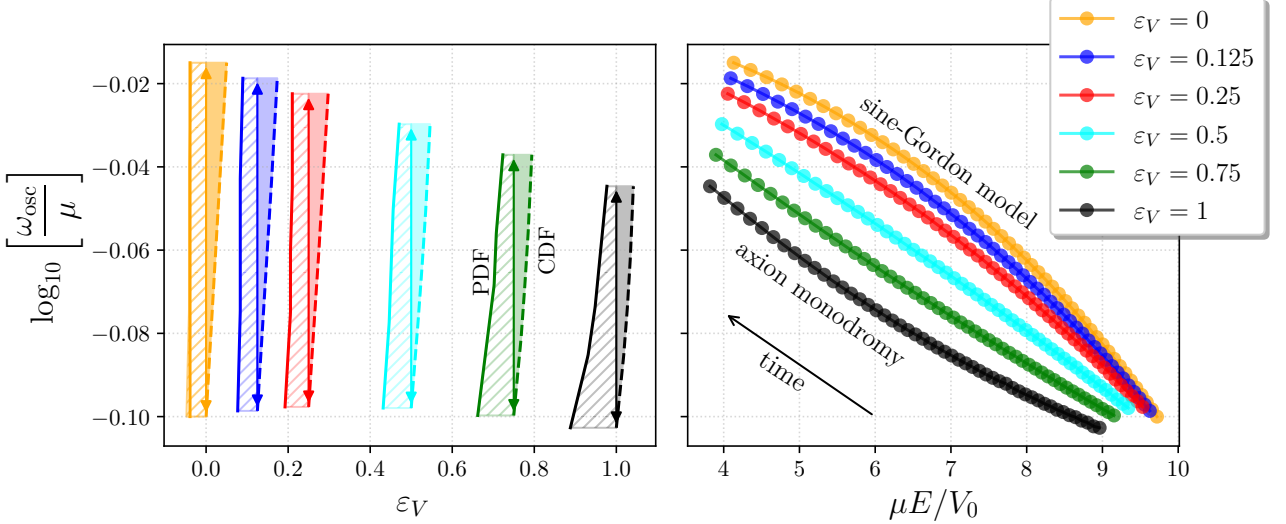


FIG. 13. Left panel: Deformation of the oscillation frequency interval as a function of  $\varepsilon_V$ . The areas shaded with lines correspond to the probability distribution functions, while the areas in semi-transparent colors determine the cumulative distributions. As the frequency intervals contracts with the curvature growth of the sine-Gordon potential, a uniformly distributed sample in  $\log_{10}(\omega_{\text{osc}}/\mu)$  deforms to have a higher number of available states at lower frequencies. Right panel: Continuous deformation of energy versus oscillation frequency curves for various intermediate stages of the potential deformation. For small values of  $\varepsilon_V$ , we observe the same concurrence to the energy vs. frequency curve for SG breathers, which is consistent with the small dimensional deformations in Fig. 6.

by the one-dimensional reduction of Eqns. (15) and (16), yielding

$$\rho(x, t) = \frac{1}{2} \left( \frac{\partial \phi}{\partial t} \right)^2 + \frac{1}{2} \left( \frac{\partial \phi}{\partial x} \right)^2 + V(\phi), \quad (29)$$

$$\frac{E}{\mu V_0} = \int_{-R_{\text{max}}}^{R_{\text{max}}} \rho(x, t) dx, \quad (30)$$

here the potential  $V(\phi)$  follows from Eqns. (22) and (23). One dimensional solutions need longer evolution times to finish the initial transient phase, where most of the classical radiation is released. Hence, the solutions are evaluated up to  $T_{\text{max}} = 2 \times 10^4 \mu^{-1}$  (which is twice the evolution time considered to produce the maps in Fig. 3 for dimensional deformations) to ensure convergence into a state of slow (and small) energy dissipation. For solutions oscillating around the potential well centered at  $\phi = 0$ ,  $\omega_{\text{osc}}$  is approximately insensitive to changes in the initial phase, thus we fix  $\theta_0 = 0$  in all the simulations.

After spanning a uniform distribution (in  $\log_{10} \omega_{\text{ini}}/\mu$ ) of 50 breathers with different initial frequencies, we report the availability of states as a function of  $\varepsilon_V$  and the energy in the two panels of Fig. 13. In the left panel, we plot two types of distributions as functions of the deformation parameter  $\varepsilon_V$ : to the left of the two-headed arrow, we plot the probability distribution shaded in colored lines. To the right, we show the cumulative distribution function shaded in semi-transparent colors for several different values of  $\varepsilon_V$  in the range  $[0; 1]$ . Both probability and cumulative distribution curves (in solid lines) are constructed by a direct polynomial fit, since the default use

of violinplot does not provide an accurate representation of uniform distributions. Two-headed arrows in solid colors depict how the frequency interval shrinks as the potential curvature increases. This panel also shows the deformation of a uniform distribution in  $\log_{10}(\omega_{\text{ini}}/\mu)$  (labeled as  $\varepsilon_V = 0$  and plotted in orange) into a distribution with higher number of states at lower frequencies, such as the one in green and black for  $\varepsilon_V = 0.75$  and  $\varepsilon_V = 1.0$ . Deformations of the probability distributions stacking more solutions at lower frequencies can also be considered in the low viscosity fluid analogy discussed in Sections III and VII. The presence of higher frequency solutions here is similar to the fine filaments of fluid appearing as the  $\varepsilon$  grows.

In the right panel of Fig. 13, we emulate the constant phase results plotted in the green dotted line labeled as  $\varepsilon = 0.5$  in Fig. 3, but now parameterized with respect to the oscillon energy. We report the availability of states as a function of energy for the same values of  $\varepsilon_V$  reported in the left panel, where we do not detect any sudden transitions or frequency ‘jumps’. Our findings are quite similar to the results presented for the perturbative regime of dimensional deformations in Fig. 6: for small values of  $\varepsilon_V$ , SG breathers are good approximate solutions of the oscillons since convergence to the  $\varepsilon_V = 0$  case still occurs. Visually, the absence of wide and squared initial breathers seems to help in making the convergence nearly uniform in this case. Moreover, we cannot detect significant changes in the spacing between adjacent states as  $\varepsilon_V$  grows and energies become smaller. Up to some extent, this is consistent with the absence of a lower energy bound for oscillon

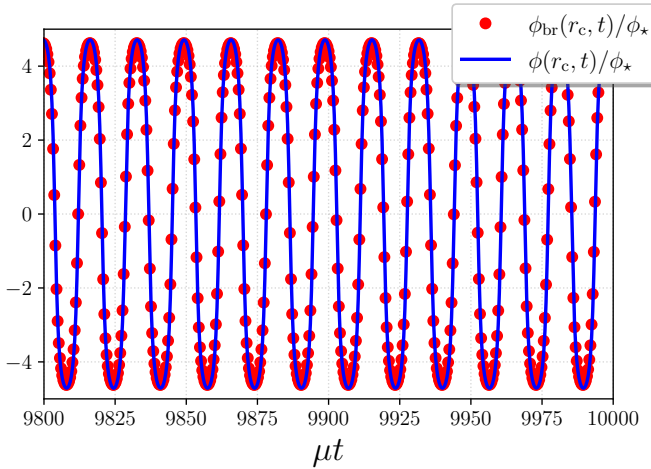


FIG. 14. Comparing the evolution of the solution of Eqns. (32) and (33) (labeled as  $\phi(r_c, t)/\phi_*$  and plotted in a solid blue line) transitioning from 3D to 1D in a couple of oscillations with a SG breather evaluated at constant  $r_c = 0.4\mu^{-1}$ . SG breather (labeled as  $\phi_{\text{br}}(r_c, t)/\phi_*$  and plotted in red dots) is a good fit of the solution considering a phase of  $\theta_{\text{br}} \approx -4\pi/21$ .

formation, which is more evident in the  $\varepsilon_V \rightarrow 0$  limit. In addition to this, the results in both panels provide sufficient evidence to show that the transition deforming the sine-Gordon (in orange) to the axion monodromy potential (in black) is smooth. As a consistency check, we can compare the orange curve corresponding to pure SG breathers ( $\varepsilon_V = 0$ ) with the energy versus oscillation frequency plot in Fig. 6, where we notice that all the dimensionally deformed cases converge to the curve in semi-transparent orange dots.

## VI. TIME-DEPENDENCE IN THE NUMBER OF SPATIAL DIMENSIONS

One way to interpret the dimensional deformations discussed in Sections III and IV is as an instantaneous modification of the sine-Gordon field equations deforming the breather solution. In this section, we explore dimensional modifications of the SG model having a finite duration. It is, therefore, valid to evaluate how the duration of the deformation modifies the structures presented in Fig. 3. To model a time-dependent dimensional transition, we start by considering the action

$$S_{\varepsilon_t} = \int \left\{ \frac{1}{2} \left( \frac{\partial \bar{\Phi}}{\partial \bar{t}} \right)^2 - \frac{1}{2} \left( \frac{\partial \bar{\Phi}}{\partial \bar{r}} \right)^2 - (1 - \cos \bar{\Phi}) \right\} \bar{r}^{\varepsilon_t} d\bar{r} d\bar{t} \quad (31)$$

which yields the equations of motion in (9) and (10) after a straightforward application of the variational principle for time-independent values of  $\varepsilon_t$ . Upgrading  $\varepsilon_t$  to a time-dependent function is, therefore, an alternative way to introduce that deformation preserving Lorentz invari-

Cases	duration $\sigma_t[\mu^{-1}]$	# of oscillations	# of decaying states
$\sigma_t^{(1)}$	0.1	[0.02; 0.16]	1080
$\sigma_t^{(2)}$	0.5	[0.1; 0.8]	1080
$\sigma_t^{(3)}$	2.5	[0.5; 4.0]	1183
$\sigma_t^{(4)}$	12.5	[2.5; 20.0]	984

TABLE II. Cases and duration (range of the number of oscillations, given the span in  $\omega_{\text{ini}}$ ) of the transitions from one to two spatial dimensions. The right column contains the number of rapidly decaying solutions obtained in the maps of Fig. 15, corresponding to the colored in brown.

ance. Introducing a such a dependence on real (instead of integer) values in the action is akin to the dimensional regularization procedure applied in quantum field theories [41–43]. After this redefinition, equations of motion follow from the functional derivative of (31):

$$\frac{d\bar{\Phi}}{dt} \equiv \bar{\Pi}_\varepsilon, \quad (32)$$

$$\frac{d\bar{\Pi}_\varepsilon}{dt} = -\bar{\Pi}_\varepsilon \dot{\varepsilon}_t \ln r + \frac{\varepsilon_t}{r} \frac{\partial \bar{\Phi}}{\partial r} + \frac{\partial^2 \bar{\Phi}}{\partial r^2} - \sin \bar{\Phi}, \quad (33)$$

where we dropped the bars for conciseness in the notation. It is clear that in the case  $\dot{\varepsilon}_t = 0$  the equations reduce to spherically symmetric in  $(1 + \varepsilon_t)$  spatial dimensions. The term proportional to  $\dot{\varepsilon}_t$  is singular at  $r = 0$ , but this is not a reason of concern since (a) the singularity is less severe than  $r^{-1}$  and (b) it is only switched on during the transition.

As for the functional form of  $\varepsilon_t$ , we continuously connect constant values of  $\varepsilon$  by using tapered cosine functions [44]. Thus, we can write  $\varepsilon_t$  as

$$\varepsilon_t = \begin{cases} \varepsilon_{\text{ini}} + \Delta D \left[ \sin \left( \frac{\pi t}{2\sigma_t} \right) \right]^2, & 0 \leq t < \sigma_t, \\ \varepsilon_{\text{ini}} + \Delta D, & t \geq \sigma_t, \end{cases} \quad (34)$$

which is a  $C^1$  piecewise function continuous at  $t = \sigma_t$ . This function is very similar to a continuous step function, except that the input and output are exact instead of asymptotic, which allows us to be precise about the initial and/or final state of the dynamical system.  $\sigma_t$  is the duration of the transition from  $D = \varepsilon_{\text{ini}} + 1$  to  $D = \varepsilon_{\text{ini}} + \Delta D + 1$  spatial dimensions, and it determines the speed of the dimensional deformation.  $\varepsilon_{\text{ini}}$  is the initial value of  $\varepsilon_t$  and  $\Delta D$  is the change in the number of spatial dimensions we want to achieve. The positive/negative sign of  $\Delta D$  is used to denote if the transition is an increase/decrease in  $\varepsilon_t$ .  $\dot{\varepsilon}_t$  is a single-peaked function of time, which becomes a “delta kick” in the limit  $\sigma_t \rightarrow 0$ . In the single-particle reduction of our system, such a spike can lead us to fractional kinetic energy gain or loss, similar to the scenario of an inelastic collision.

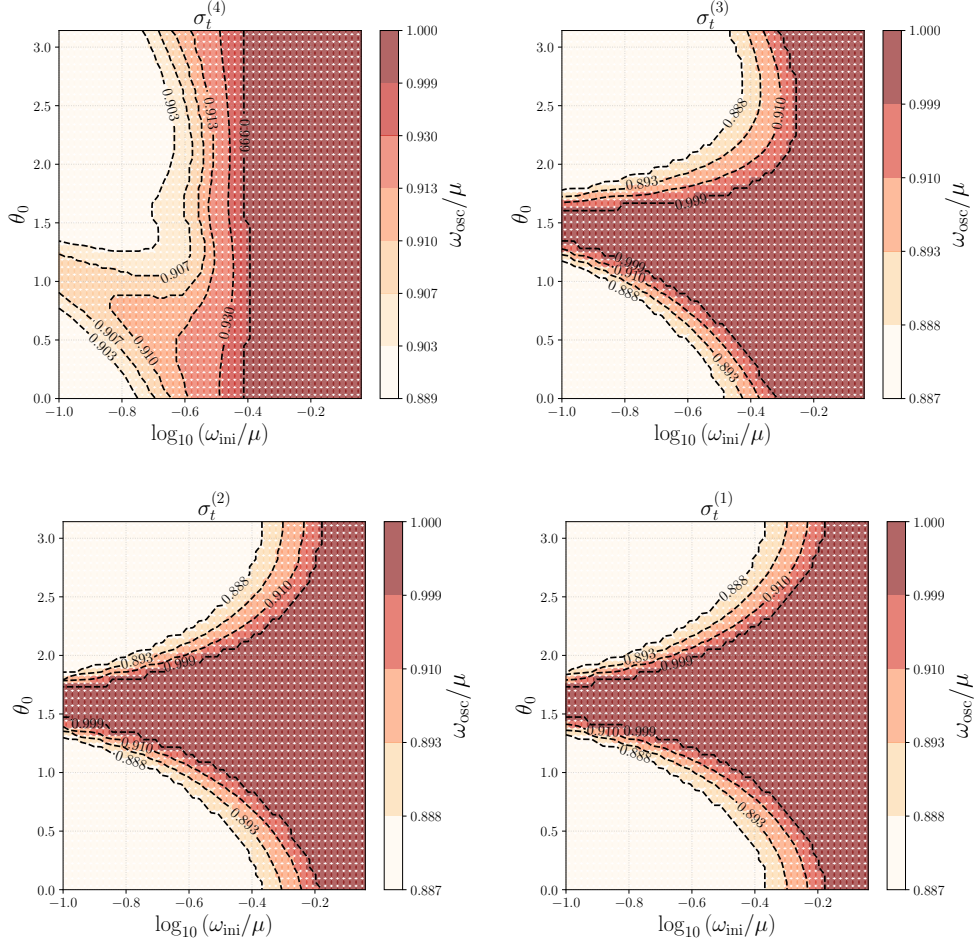


FIG. 15. Frequency of the oscillon as a function of the phase and frequency of the initial SG breathers for time-dependent transitions from one to two spatial dimensions. We considered the transition durations reported in Table II. The cusps reported in Fig. 3 emerge in the limit of abrupt dimensional transitions, such as the two panels at the bottom, and conversely become less sharp as the transition slows down (i.e., the two panels at the top). In all scenarios, rapidly decaying states represent 40% (approx.) of the 2500 solutions evolved. Symmetry around  $\theta_0 = \pi/2$  is only restored in the limit  $\sigma_t \rightarrow 0$ .

As a proof of concept for the deformed field equations, we evaluate the transition from a breather-like spherically symmetric oscillon in three spatial dimensions to a 1D SG breather. In this case, the initial condition has the same shape of the breather in Eqns. (24) and (25) with  $\omega_{\text{ini}} = 0.1\mu$  and initial phase  $\theta_0 = 0$ . To represent the dimensional transition, we use  $\varepsilon_{\text{ini}} = 2$ ,  $\Delta D = -2$  and  $\sigma_t = 0.1\mu^{-1}$  in Eq. (34), which is approximately instantaneous. Fig. 14 shows that the solution evaluated at constant radius  $r_c = 0.4\mu^{-1}$  can be written as

$$\frac{\phi_{\text{br}}(r_c, t)}{\phi_*} = 4 \tan^{-1} \left[ \frac{\sqrt{1 - \omega_{\text{br}}^2} \cos(\omega_{\text{br}} t - \theta_{\text{br}})}{\omega_{\text{br}} \cosh(\sqrt{1 - \omega_{\text{br}}^2} r_c)} \right], \quad (35)$$

with  $\theta_{\text{br}} \approx -4\pi/21$  and  $\omega_{\text{br}} = \omega_{\text{osc}} \approx 0.381\mu$ . The value of  $\omega_{\text{br}}$  was extracted from the evolving field following the procedure described in Subsec. II A (as seen in the right panel of Fig. 1): by finding the dominant frequency of the solution evaluated at constant radius  $r_c$ . As plotted in the

figure, this result is fully consistent with a well-known fact of the sine-Gordon model [10]: its solutions can only be combinations of breathers, solitons and non-linear waves. Simultaneously, we evaluated the consistency of the deformed field equation solutions with SG breathers, and validated the frequency extraction procedure explained in Fig. 1.

It is reasonable to evaluate the sensitivity of the oscillation frequency ( $\omega_{\text{osc}}$ ) with the dynamical dimensional transition suggested in Eqns. (32) and (33). None of the breathers has been deformed to compensate for the lack of energy in the one-dimensional initial conditions. Considering  $\varepsilon_{\text{ini}} = 0$  and  $\Delta D = +1$ , we simulate the dynamical deformation of 1D breathers into 2D oscillons for the four different durations reported in Table II. As we can notice, the first two cases  $\sigma_t^{(1)}$  and  $\sigma_t^{(2)}$  correspond to transitions happening in less than one oscillation. Cases  $\sigma_t^{(3)}$  and  $\sigma_t^{(4)}$  last more than a full oscillation period, observing

that  $\sigma_t^{(1)}$  and  $\sigma_t^{(4)}$  are different by two orders of magnitude. We generate oscillation frequency maps in Fig. 3 in the same range of initial frequencies and phases used in the perturbative regime. In the four panels of Fig. 15, we present the oscillation frequency maps corresponding to the transition durations in the table. Observing that the symmetry of the cusp centered at  $\theta_0 = \pi/2$  is only restored in the abrupt transition limit (in the lower right and left panels labeled as  $\sigma_t^{(1)}$ ), used throughout the perturbative (in Sec. III) and non-perturbative (in Sec. IV) correction regimes discussed in this manuscript. An important observation to remark is that, essentially, the oscillation frequency range is (approx.) independent of the dimensional transition duration, matching the instantaneous limit. Moreover, the right column of Table II reveals that the number of rapidly decaying solutions (in brown dots) varies in less than 10% for a two orders of magnitude change in the transition duration, which implies that the availability of states is also approximately independent of the transition speed. However, it would not rigorous to conclude the same considering different choices of initial conditions. Similar deformations to the high duration maps  $\sigma_t^{(3)}$  and  $\sigma_t^{(4)}$  in Fig. 15 can be reproduced if we change the initial frequency binning of the  $\sigma_t^{(1)}$  panel, by mixing some fraction of the amplitude evolution from adjacent initial frequencies. For larger time intervals, such as in the panel labeled as  $\sigma_t^{(4)}$ , the cusps become less sharp to the point of becoming smooth for adiabatic dimensional transitions. It is clear that the initial dependence tends to disappear as the transitions becomes slower. As shown in Table II, the smallest transition speed has a relatively mild effect in changing the number of available states. Nonetheless, the same cannot be said about the amount of intermediate frequency states. In the same panel, we notice that the frequency gradient becomes smoother, and consequently, the number of amplitude modulated solutions increases with respect to the other cases.

## VII. DISCUSSION

In this paper, we deform the breather solution of the sine-Gordon equation to produce standing oscillons. Such a deformation consists of promoting the two spatial derivatives of the 1D equation to the  $D$ -dimensional Laplacian in spherical symmetry. Via the auxiliary parameter  $\varepsilon \equiv D - 1$ , we treat the number of spatial dimensions as a real control parameter, which (a) modifies the first-derivative correction of the field equations, and (b) separates the perturbative – i.e., when  $\varepsilon > 1$  – from the non-perturbative – i.e., in  $\varepsilon \in [1; 2]$  – regime of SG model deformations. Other promising approaches study deviations from integrability [29–32] and the weak symmetry breaking via minor violations in the conservation laws seen in some of the loop-algebra charges.

In Section III, we study the perturbative regime of

dimensional deformations of the SG breather solution by considering the breather state in Eqns. (6–8) as initial conditions of the modified SG model. Even when oscillons are known to be multi-frequency objects, we consider  $\omega_{\text{osc}}$  as a diagnostic parameter, which is the dominant frequency in the time series tracing the value of the solution at the center  $r = 0$ . Along with the oscillon energy, the oscillation frequency can be used to distinguish if a stable solution has formed or not. Scanning over the initial oscillation frequency  $\omega_{\text{ini}}$  and phase  $\theta_0$ , we find in Fig. 3 a preference to form oscillons from collapsing shells having more potential than kinetic energy. The range of oscillation frequencies compresses as  $\varepsilon$  grows. In addition to this, the maps in Fig. 3 contain a sufficiently large amount of simulations to effects of the number of spatial dimensions in the availability of stable spherically symmetric oscillons. Our results are reported in Fig. 5, where we show that for small values of  $\varepsilon$ , the distribution of states is unimodal and centered towards lower frequencies, which is reasonable since we are considering a non-trivial amount of solutions deformed from long and squared breathers. As the number of spatial dimensions grows, the distributions become bimodal to accomodate a large number of field configurations, which either decay rapidly or become orders of magnitude wider than their original breather-like initial conditions. The constant phase level curve plotted in green dots in the  $\varepsilon = 0.5$  shows how the oscillation frequency ( $\omega_{\text{osc}}$ ) after a few hundred oscillations depends on the initial breather frequency. This function can be translated into an energy dependence to represent the dynamical state of the oscillating field. In agreement with many previous results, such as [36–38], our results in Fig. 6 show several states with small energies, with no signs of a lower energy bound. In addition to this, the convergence of energy versus frequency curves for small values of  $\varepsilon$  shows that oscillons are well-approximated by sine-Gordon breathers oscillating in  $D = 1 + \varepsilon$  spatial dimensions, only for sufficiently small values of  $\varepsilon$ . In Section V, we evaluate the oscillation frequency dependence on the solution energy, as well as changes in the availability of states after potential deformations. We progressively modify the SG potential well centered at  $\phi = 0$  to the 1D axion monodromy model in order to extend our results beyond dimensional deformations. Up to some extent, our findings are similar with the results reported in the perturbative regime, with no evidences of a lower energy bound to form stable oscillons, especially in the case of small potential deformations.

Smooth frequency gradients in the scan over initial breather parameters reported in Fig. 3 ( $\varepsilon = 0.75$ ) show the presence of solutions with amplitude modulations. These solutions (presented with more detail in the three panels of Fig. 4) appear in regions of initial parameter space which separate stable from rapidly decaying field configurations. Radial profile evolution shows intermittent phases of contraction and expansion of the oscillon's core due to the emission of classical radiation in a countable number of bursts. Intermittent phases of amplitude

modulation are not an artifact of equations of motion in spherical symmetry, in Fig. 18 we report the evolution of a two-dimensional oscillon showing the same intermittent behavior. In two spatial dimensions, amplitude modulation appears in a broad range of the initial parameter space: the modulation frequency decreases as the initial breather becomes smaller. Possibly, such modulation is a sign of an emergent time scale in the problem, which becomes dominant as bound states decay. The existence of these solutions complicates the design of a system of many interacting oscillons fully consistent with energy equipartition. We suspect (but still cannot confirm) that these solutions are related to the staccato oscillating fields discussed in [19, 20].

The next reasonable step is to extend our analysis to  $\varepsilon > 1$  regime. In Section IV, we notice that the energy budget is not sufficient if one wants to produce oscillons out of breathers in two or three spatial dimensions. Therefore, it is convenient to modify the parameterization of initial conditions to inject more energy into the system. One of the simplest ways to do this is to boost the field's amplitude by multiplying the SG breather solution by a number, as suggested in Eq. (18). The expression Eq. (19) describes a flow line of initial parameters relating the growth in amplitude and initial breather frequency. Such a flow line crosses transversally constant energy surfaces, which we follow to find that the smooth incline containing an indefinite number of low-energy states in the perturbative regime collapsed into a single rapidly-decaying solution. The phase transition from unstable to stable solutions becomes sharper as the number of spatial dimensions grows. In the low-energy limit, the deformations only allow two distinct states, and the role of oscillating solutions showing intermittent contraction and expansion phases/amplitude modulation is to connect both solutions, which can be noticed in Fig. 8. Differences between the perturbative and the non-perturbative regime become clearer after observing oscillon distributions in Fig. 6, and in the left panels of Fig. 9. Both are plotted with respect to the energy (initial and post-transient) and the oscillation frequency  $\omega_{\text{osc}}$ . With the increase of  $D$ , the smooth incline of low energy states formed in the perturbative case (with no apparent low-energy bound) collapses to a single rapidly-decaying solution in  $D \geq 2$  spatial dimensions. This has practical implications in future research: it is not possible to build oscillons in two or three spatial dimensions from a single parameter solution, such as the SG breather. Semi-analytical oscillons suggested in [24] need from additional parameters to be increase the solution's energy before being renormalized. Nonetheless, the renormalization procedure and further predictions of long-lived states are possible in the perturbative regime considering the SG breather as a background solution. As for the extension of parameter space to increase the initial state energy, one must proceed with caution since increments in amplitude cannot be unbounded. In Fig. 12, we learn that a generic injection of energy does not certify an increase in the stability of an oscillon. Boosting the

initial energy in two orders of magnitude yields a series of contracting and expanding spherical shells of different sizes decaying after a few oscillations around different potential minima. Clearly, there is not enough binding energy to keep all of the collapsing energy shells localized within a localized region.

As for the critical energy as a function of the problem's dimensionality, the upper panel of Fig. 11 shows that it is not possible to represent the critical energy by a single power law, the values in Table I make this more evident by showing that perturbative and non-perturbative cases run with different powers of  $D$ . Nevertheless, the lower panel of the same figure shows that the oscillation frequency fits in a single power law running as  $\varepsilon^{1/8}$ . SG breathers can also be continuously deformed into oscillons from other potentials, as suggested in Section V, by deforming sine-Gordon breathers into axion monodromy oscillons in one dimension. As a complement of our results for  $\varepsilon > 1$  in Sec. IV, Section VI explores the possibility of continuous time-dependent dimensional transitions introduced from the field's action. Our findings not only explain why the cusps around  $\theta_0 = \pi/2$  in  $\omega_{\text{osc}}$  appear in Fig. 3 are caused by non-adiabatic transitions in the number of spatial dimensions. These also suggest that the abundance of solutions undergoing intermittent phases of expansion and contractions of the core can be tuned by changing the duration of the dimensional transition. For the initial states used, oscillation frequency ranges are insensitive to (non-)adiabatic dimensional transitions. Moreover, it is also reasonable to introduce curvature corrections by considering  $\varepsilon_V$  to be a time-dependent function, following the same logic as in Sections V and VI. Potentially, we could emulate the spontaneous emergence of corrections in the potential. In a similar way, it would be interesting to extend this methodology beyond oscillons and consider other localized structures, such as solitons and strings produced by topological defects [45–47], finding their connections (if any) with other integrable models.

## ACKNOWLEDGMENTS

The authors would like to thank J. Richard Bond, John Dubinski, Andrei Frolov, Daniel Horna, Lorena Luján, Thomas Morrison, Levon Pogosian, Guillermo Quispe and Leo Stein for many fruitful conversations, technical and logistic support, and their valuable feedback in earlier versions of this paper. All of the computations were performed on the computing workstations at the Canadian Institute for Theoretical Astrophysics (CITA). The work of JG was partially supported by the Natural Sciences and Engineering Research Council of Canada (NSERC), funding reference #CITA 490888-16, #RGPIN-2019-07306. The work of JB was partially supported by the Natural Sciences and Engineering Research Council of Canada (NSERC) and by the Simons Modern Inflationary Cosmology program.

## Appendix A: Numerical setup and convergence

In this paper, oscillons are build as standing spherically symmetric solutions of the deformed sine-Gordon model. Here we describe the pseudospectral numerical setup used to solve the field equations in Eqns. (9) and (10), showing the numerical implementation to find the field solutions and the spectral/spatial convergence tests performed. In particular, convergence tests are applied to oscillons undergoing phases of expansion and contraction of their cores.

### 1. Differential operators and the spectral grid

Field equations are solved in the radial semi-infinite domain  $r \in (0; \infty)$ , which we construct using the Gauss-Lobatto grid

$$\theta_i = \left( n - i + \frac{1}{2} \right) \frac{\pi}{n}, \quad r_i = \ell \cot \frac{\theta_i}{2}, \quad (\text{A1})$$

implemented in  $n$  nodes collocated to spread the numerical error (approx.) evenly along  $\ell$ . In our case,  $\ell$  is set as the size of the largest oscillon we can resolve. The implementation of the spectral lattice is similar to [48]; the only difference is the factor of 1/2 from the argument in the RHS, selecting the even Chebyshev polynomials as basis functions instead of the whole set. As implemented in (A1), the cotangent mapping excludes  $r = 0$  to avoid singularities introduced after including explicitly the term proportional to  $1/r$  and the radial derivative as a modification to the SG model. As discussed by Boyd in [49], the expansion in Chebyshev polynomials is not different from a cosine transform. Therefore, a target function  $f$  expandable in the polynomial basis can be expressed as

$$f(r_i) = \sum_{n \in \mathbb{N}} c_n \cos [n\theta(r_i)], \quad (\text{A2})$$

where  $\theta(r_i)$  follows from (A1)

$$\theta(r_i) = 2 \cos^{-1} \left( \frac{r_i}{\sqrt{r_i^2 + \ell^2}} \right). \quad (\text{A3})$$

Thus, we can write the derivative of the target function as

$$\frac{df(r_i)}{dr} = \sum_{n \in \mathbb{N}} \left[ -nc_n \frac{d\theta(r_i)}{dr} \right] \sin [n\theta(r_i)], \quad (\text{A4})$$

which implies that the term inside squared brackets is the sine transform ( $\mathcal{F}_{\sin}$ ) of the radial derivative. Consequently, the radial derivative is also equivalent to the following inverse sine transform

$$\frac{df(r_i)}{dr} = \frac{2\ell}{\ell^2 + r_i^2} \mathcal{F}_{\sin}^{-1}(nc_n) \quad (\text{A5})$$

if we use `fftw3` [50] to compute cosine/sine transforms, the elements of the  $nc_n$  array need to be rearranged before applying an inverse sine transform. The rearrangement shifts the array indices by one (for example: index  $m$  becomes  $m + 1$ ) and replaces the first element by zero. An important advantage of this approach is the reduction of the computational cost from  $2N^2$  (corresponding to optimized matrix multiplication) to  $2.5N \log_2 N$  [49], which represents an important boost in speed compared to the algorithm suggested in [48] and allows us to explore a large number of field realizations. The cotangent mapping can be freely exchanged to other coordinate choices specific to the problem. In addition to this, as in every (pseudo-)spectral approach, the precise calculation of integrals along the whole frequency domain is a much simpler task, since all we need is the zeroth frequency component of the cosine transform of a function,

$$\int_0^\infty g(r) dr = \frac{\pi}{2} \sum_{n \in \mathbb{N}} \left( \frac{r_n^2 + \ell^2}{\ell} \right) g(r_n), \quad (\text{A6})$$

given by the RHS of this equation after being remapped in the radial grid. This is of special importance to compute the energy of the oscillon, specified in (15) and (16) as a diagnostic parameter to determine the dynamical state of the solution. There is no need to compute the FT explicitly since this means a  $\log N$  penalty. We advice to proceed with caution, since the complete exclusion of matrix multiplication operations is only recommendable when interpolations/extrapolations of the solution inside/outside its domain are not required.

As for the time evolution, we used an eighth-order Gauss-Legendre symplectic integrator [51], which is the same used in [24, 48], where the time step for the evolution is limited by the Courant-Friedrichs-Lowy (CFL) condition:

$$\Delta t_{\text{CFL}} \approx \frac{\Delta x_{\min}}{2\pi}, \quad (\text{A7})$$

this condition holds for semi-linear wave equations bounded potentials (and external) interactions in the equations of motion.

### 2. Perfectly matched layers (PMLs) and equations of motion in flux conservative form

As discussed and shown in different instances of the paper (such as in Figs. 4 and 12), oscillons dissipate energy throughout their entire evolution. Outgoing bursts of classical radiation come from the scattering part of the solution. These need to be removed from the simulation box to prevent unphysical self-interactions with the oscillating core. Using (and processing) of large simulation boxes involves memory-intensive processes, and does not need a large number of simulations to become computationally unaffordable when we manage long-lived solutions, such as oscillons. In [52], we find a practical method to implement absorbing boundary conditions which is amenable

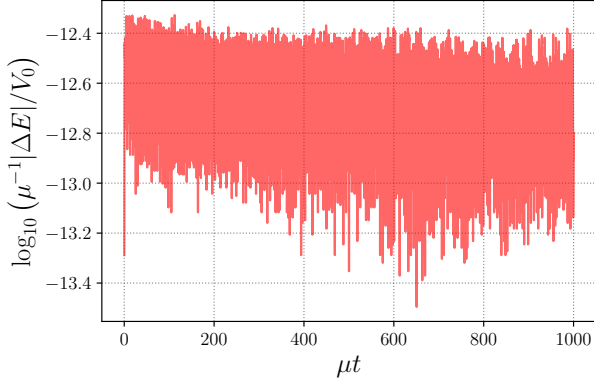


FIG. 16. Energy conservation for a standing sine-Gordon breather with  $\omega_{\text{ini}} = 0.794\mu$  and  $\theta_0 = 0$ , evolved from the equations of motion (A19)–(A22) in the case  $\varepsilon = 0$ . Showing that perfectly matched layers do not interfere with the solution inside the simulation length.

to solve oscillon evolution. Its implementation requires to rewrite

$$\frac{d\Phi}{dt} = \Pi_\Phi, \quad (\text{A8})$$

$$\frac{d\Pi_\Phi}{dt} = \left[ \frac{\partial^2}{\partial r^2} + \frac{\varepsilon}{r} \frac{\partial}{\partial r} \right] \Phi - \sin \Phi, \quad (\text{A9})$$

which is the same as in Eqns. (9) and (10) (bars omitted for conciseness), in flux conservative form.

Recalling that  $\Phi$  has units of  $\phi/\phi_*$ , we can follow the procedure developed in [48] to define the auxiliary variable  $v \equiv r^{-1}\partial_r\Phi$ . Such a variable redefinition reduces the order of spatial derivatives and preserves the reflection symmetry of the solution around the axis  $r = 0$ , making the system equivalent to

$$\frac{d\Phi}{dt} = \Pi_\Phi, \quad (\text{A10})$$

$$\frac{d\Pi_\Phi}{dt} = \left[ r \frac{\partial}{\partial r} + (\varepsilon + 1) \right] v - \sin \Phi, \quad (\text{A11})$$

$$\frac{dv}{dt} = \left[ \frac{1}{r} \frac{\partial}{\partial r} \right] \Pi_\Phi, \quad (\text{A12})$$

here the last equation is a consistency condition enforcing the commutation of time and radial derivatives acting on  $\Phi$ . If we consider an additional auxiliary variable such that

$$\frac{dw}{dt} = (\varepsilon + 1)v - \sin \Phi, \quad (\text{A13})$$

the field equations can be written in flux conservative

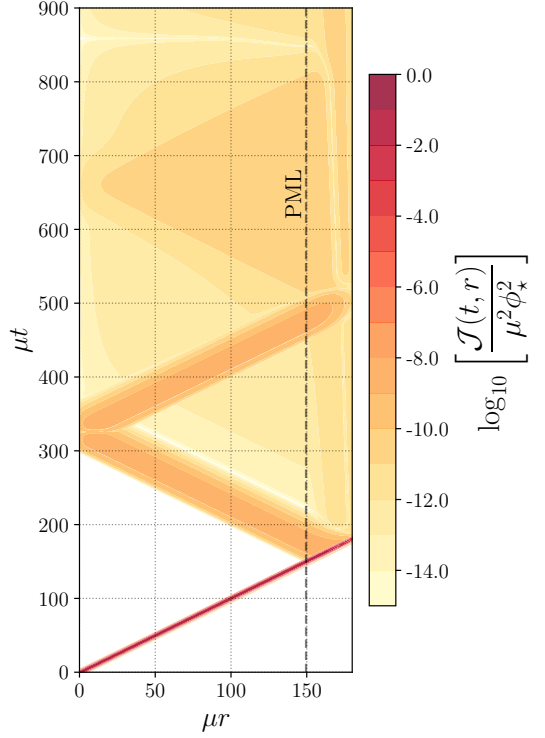


FIG. 17. Impact of a Gaussian wave packet on a PML. Scalar flux reduces in 9–10 orders of magnitude after hitting the absorbing layer for the first time, which suggests that the setup is operational.

form as follows

$$\frac{d\Phi}{dt} = \Pi_\Phi + w, \quad (\text{A14})$$

$$\frac{d\Pi_\Phi}{dt} = r \frac{\partial v}{\partial r}, \quad (\text{A15})$$

$$\frac{dv}{dt} = \left[ \frac{1}{r} \frac{\partial}{\partial r} \right] (\Pi_\Phi + w), \quad (\text{A16})$$

$$\frac{dw}{dt} = (\varepsilon + 1)v - \sin \Phi, \quad (\text{A17})$$

after redefining the time derivative by a shift  $\Pi_\Phi - w \rightarrow \Pi_\Phi$ . One of the advantages of the flux conservative form is order reduction in the number of spatial derivatives. The implementation of perfectly matched layers is based on the analytical continuation of the simulation domain, resulting in the deformation of the radial derivative

$$\frac{\partial}{\partial r} \rightarrow \frac{1}{\left( 1 + \frac{\gamma(r)}{\partial_t} \right)} \frac{\partial}{\partial r} \quad (\text{A18})$$

where  $\gamma(r)$  is zero along the simulation length and behaves as a smooth incline in the last nodes of the grid, acting as an absorbing layer.

Once the derivative redefinition is applied in the Eqns. (A15) and (A17), we find the set of equations to

simulate

$$\frac{d\Phi}{dt} = \Pi_\Phi + w, \quad (\text{A19})$$

$$\frac{d\Pi_\Phi}{dt} = r \frac{\partial v}{\partial r} - \gamma \Pi_\Phi, \quad (\text{A20})$$

$$\frac{dv}{dt} = \left[ \frac{1}{r} \frac{\partial}{\partial r} \right] (\Pi_\Phi + w) - \gamma v, \quad (\text{A21})$$

$$\frac{dw}{dt} = (\varepsilon + 1)v - \sin \Phi. \quad (\text{A22})$$

Hence, we have doubled the number of equations to evolve. Writing flux conservative equations for the one-dimensional deformed system in Sec. V and the time-dependent dimensional transitions in Sec. VI is not substantially different from the procedure described above. In the latter case, we also need one more equation corresponding to an auxiliary variable  $\psi$ , defined to evolve as

$$\frac{d\psi}{dt} = \dot{\varepsilon}_t \Pi_\Phi, \quad (\text{A23})$$

to absorb the inelastic collision term in (33). After redefining the time derivative by  $\Pi_\Phi + \psi \ln r - w \rightarrow \Pi_\Phi$ , the equations of motion with absorbing boundary layers can be written in their final form,

$$\frac{d\Phi}{dt} = \Pi_\Phi + w - \psi \ln r, \quad (\text{A24})$$

$$\frac{d\Pi_\Phi}{dt} = r \frac{\partial v}{\partial r} - \gamma \Pi_\Phi, \quad (\text{A25})$$

$$\frac{dv}{dt} = \left[ \frac{1}{r} \frac{\partial}{\partial r} \right] (\Pi_\Phi + w - \psi \ln r) - \gamma v, \quad (\text{A26})$$

$$\frac{dw}{dt} = (\varepsilon_t + 1)v - \sin \Phi, \quad (\text{A27})$$

$$\frac{d\psi}{dt} = \dot{\varepsilon}_t (\Pi_\Phi + w - \psi \ln r), \quad (\text{A28})$$

which is the extension of Eqns. (A19–A22) for the case of time-dependent dimensional transitions.

For consistency, we evaluate energy conservation in the simulation length by considering the case  $\varepsilon = 0$  (i.e., during the oscillation of standing breathers). In Fig. 16, we plot the energy conservation residuals  $|\Delta E| \equiv |E(t) - E(t_0)|$ , observing that conservation holds at the level of round-off errors in double precision, and residuals do not grow in time. Evidencing that perfectly matched layers do not affect the solution dynamics inside the simulation volume. Additionally, it is important to show the effect of PMLs as filters of radiation escaping the simulation length. To do so, we allow the propagation of a free Gaussian wavepacket following the one-dimensional wave equation and compute its scalar flux

$$\frac{\mathcal{J}(t, r)}{\mu^2 \phi_\star^2} \equiv \frac{\partial \Phi}{\partial r} \frac{\partial \Phi}{\partial t}, \quad (\text{A29})$$

in the simulation domain. In Fig. 17, we observe the absorption of the Gaussian peak “fired” directly towards the

PML. Reflected scalar flux is several orders of magnitude smaller compared to the ingoing flux, and becomes even smaller with posterior reflections. A closer look at the red region shows that the solution decays progressively as it goes through the absorbing layer.

It is important to set the boundary layer in a way that there are sufficient points to resolve properly the dynamics of exponential damping. For the specific case of oscillons with scattering solutions decaying with fractional powers of  $1/r$  requires to locate the layer sufficiently close to absorb the whole train of outgoing radiation without affecting spectral convergence. At the same time, absorbing layers cannot “invade” the region where the localized solution oscillates. The asymptotic behavior in Eq. (13) only gives a crude estimate on the correct position of the PML, where  $\gamma(r) \neq 0$ , and also of the length scale  $\ell$ . For the largest initial breather frequency explored in this paper  $\omega_{\text{ini}} = 0.966\mu$ , the length scale is of order one since  $(1 - \omega_{\text{ini}}^2)^{-1/2} \sim 4\mu^{-1}$ . Our experience with dimensional deformations is that breather cores are stretched by at least one or two orders of magnitude as these become stable oscillons. Hence, we used  $\ell = 100\mu^{-1}$  as a reasonably safe length scale where oscillon are solved in full numerical precision. This implies that the lowest resolution simulations need  $2^{10}$  nodes (or more) to be computed with sufficient dynamical range, considering enough nodes to resolve the exponential decay of transient radiation. For consistency, we also checked that larger values of  $\ell$  have no effect in the dynamics of the solution, as long as there are enough points to resolve exponential damping inside the PML. As a comment, we attempted smaller values of  $\ell$  in order to increase the computational performance even further; but the solutions started to show small differences in the evolution due to cumulative errors in the radial derivatives. Nonetheless, the shape and ranges of the frequency maps in Fig. 3 are insensitive to variations in all of the numerical simulation parameters.

### 3. Intermittent expansion and contraction of the oscillon core in two-dimensional solutions

The presence of modulation in the oscillons amplitude is not an artifact of using radial equations of motion. Let us evaluate the two-dimensional equations of motion, given by

$$\frac{\partial \bar{\Phi}}{\partial t} = \bar{\Pi}, \quad (\text{A30})$$

$$\frac{\partial \bar{\Pi}}{\partial t} = \frac{\partial^2 \bar{\Phi}}{\partial x^2} + \frac{\partial^2 \bar{\Phi}}{\partial y^2} - \sin \bar{\Phi}, \quad (\text{A31})$$

where  $\bar{\Phi} \equiv \phi(x, y, t)/\phi_\star$  and the bars over time and space coordinates were omitted, again, for conciseness in the notation. For these results, we use an independent piece of code working with periodic boundary conditions in a two-dimensional simulation box, being this sufficiently large to avoid interactions with classical radiation. In

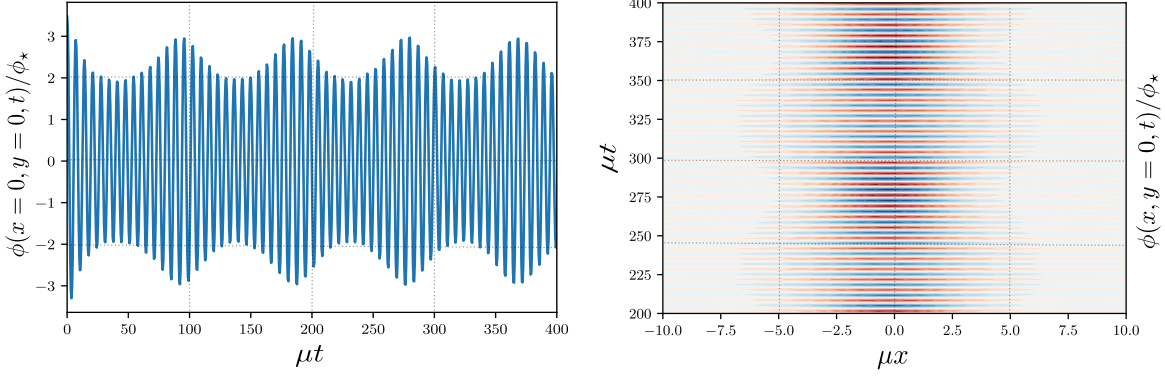


FIG. 18. Evolution of a breather-like initial condition in two-dimensional sine-Gordon model for  $\omega_{\text{ini}} = 0.63\mu$ . Left panel: Projection of the solution in the  $y = 0$  plane, showing quasi-periodic phases of contraction and expansion of the oscillon core. Right panel: Evolution of the solution in the origin, consistent with modulations in the amplitude described for the perturbative regime in Sec. III.

the right panel of Fig. 18, we show the evolution of a solution with the breather-like initial conditions in (18) projected in the  $y = 0$  plane, choosing  $\alpha = 1$  (i.e., without modifying the initial amplitude),  $\theta_0 = 0$  and  $\omega_{\text{ini}} = 0.63\mu$  to fix the initial breather's shape. The oscillon's core undergoes intermittent periods of contraction and expansion noticeable in distances comparable to the size of the object. Intermittent behavior does not seem to support energy equipartition, since during this phase radiation can be trapped and injected again before escaping the core. In the left panel of the same figure, we show amplitude modulation for the same initial breather parameters, which is also visible in the perturbative regime discussions in Sec. III. The existence of intermittent phases of contraction and expansion of the oscillon core (represented by amplitude modulations) has been tested in two independent numerical setups. Therefore, it is unlikely that these are consequences of some numerical artifact, or some long-time growing instability. Apart from this consistency check, we can also use the 2D solutions of Eqns. (A30) and (A31) at constant initial phase  $\theta_0$  to sample over different values of initial frequency ( $\omega_{\text{ini}}$ ). We noticed that the dominant frequency of the amplitude modulation envelope (similar to the red curve in right panel of Fig. 1) becomes larger as  $\omega_{\text{ini}}$  reduces, being this consistent with our observations in the perturbative regime. In principle, such a frequency can be treated as an additional diagnostic parameter, which is measurable and can be sampled over the span of initial parameters to be connected with the imaginary part of the frequency (if such a connection exists), which is the oscillon's decay rate. We will study its connections to the dynamical state of amplitude modulated solutions in a future project.

#### 4. Convergence tests

In this section, we perform convergence tests for the amplitude modulated solution depicted in the middle and

Resolutions	# of nodes	time step [ $\Delta t_{\text{CFL}}^{(\text{res})}$ ]
max	8192	1/16
mid-max	4096	1/8
mid-min	2048	1/4
min	1024	1/4

TABLE III. Resolutions used to solve Eqns. (A19)–(A22) for  $\varepsilon = 0.75$ . Considering  $\ell = 100\mu^{-1}$  and the absorbing boundary layer centered at the end of the simulation box, we perform convergence tests for the field configuration with intermittent phases of expansion and contraction shown in Fig. 4.

right panels of Fig. 4 for  $\varepsilon = 0.75$ . Considering that dimensional deformations stretch the breathers' length to form much wider oscillons, the numerical implementation needs at least  $10^3$  nodes to resolve oscillons with sufficient dynamical range. We construct four radial semi-infinite domains following the Gauss-Lobatto grids in (A1) for the length scale  $\ell = 10^2\mu^{-1}$ , and considering the resolutions reported in Table III, where the CFL time scale  $\Delta t_{\text{CFL}}$  follows from the condition in Eq. (A7), which follows from the dispersion relation for semi-linear wave equations with bounded potentials. In the left panel of Fig. 19, we plot the spectral coefficients (found by computing the cosine transform of the solution) in terms of the number of nodes for all of the resolutions at fixed time  $t = 10^4\mu^{-1}$ . We observe that keeping high frequency coefficients in the same magnitude as round-off errors requires a large number of collocation nodes. High frequency coefficients appear during the initial transient phase as scattering modes decay with fractional powers of the distance. Spectral coefficients coincide for the first hundred nodes, which are sufficient to resolve the core, as we can observe in the right panel. Up to some extent, this justifies the invariance of the oscillation frequency maps in Fig. 3 with changes in

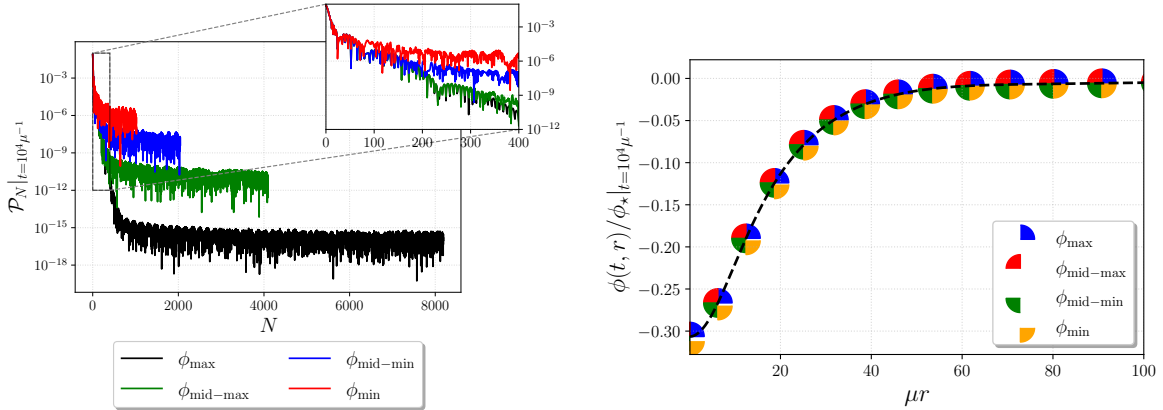


FIG. 19. Left panel: Spectral coefficients as functions of the number of collocation points, corresponding to the solution in the middle and right panels of Fig. 4 for  $\varepsilon = 0.75$ . Initial condition is the breather parameterized by  $\omega_{\text{ini}} = 0.398\mu$  and  $\theta_0 = 0.6\pi$ , we plot the solution at fixed  $t = 10^4\mu^{-1}$  for the resolutions reported in Table III. Results at all resolutions coincide for the first hundred nodes, which are sufficient to produce the oscillon core. Right panel: Oscillating field as a function of the radius for the same resolutions. The origin is where the difference between solutions is clearer; however, all of the solutions coincide with (approx.) 1% relative errors. Dashed black curve is a snapshot (at the same instant) of the solution resolved at the highest resolution.

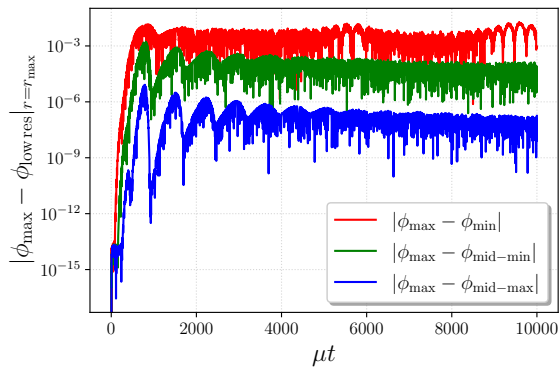


FIG. 20. Subtracting field configuration at  $r = r_{\text{max}}$ , where the differences between field configurations are the largest (this is near the origin, as depicted in the right panel of Fig. 19). Numerical error decreases as the solutions are resolved with more collocation modes.

the resolution. Solutions keeping all of the high-frequency terms with powers below machine precision are computationally expensive, needing at least 8-10 times more k-modes to be fully resolved. In the right panel, we observe the field configuration as a function of the radial

coordinate. The solutions at different resolutions (interpolated to the lowest resolution spatial grid) look almost identical: it is only at the origin where one-percent level errors can be assessed.

An important feature we can extract from the right panel of Fig. 19 is that we can evaluate the convergence errors by considering the field values at the origin (or the closest point in the collocation lattice) at different resolutions. Considering the solution at the highest resolution as a reference, we can subtract the solutions from the other resolutions and evaluate the differences as functions of time. To compare the outcomes from different spatial resolutions, the time step  $\Delta t = \Delta t_{\text{CFL}}^{\text{mid-max}}/8$  is kept as a constant in all the resolutions to avoid inaccuracies due to time interpolation. In Fig. 20, we plot the difference between field configurations obtained at different spatial resolutions. Observing that numerical errors reduce as we use more modes to resolve the oscillating configurations, this figure is a piece of evidence indicating numerical convergence. Moreover, it is important to remark that reported errors do not grow in time for the highest resolutions. As expected, for the lowest resolutions errors tend to increase when the core expands and contracts, which is the defining feature of amplitude modulated solutions.

---

[1] I. L. Bogolyubsky and V. G. Makhankov, Lifetime of Pulsating Solitons in Some Classical Models, *Pisma Zh. Eksp. Teor. Fiz.* **24**, 15 (1976).

[2] M. A. Amin, R. Easter, H. Finkel, R. Flauger, and M. P. Hertzberg, Oscillons After Inflation, *Phys. Rev. Lett.* **108**, 241302 (2012), arXiv:1106.3335 [astro-ph.CO].

[3] J. Ollé, O. Pujolàs, and F. Rompineve, Oscillons and Dark Matter, *JCAP* **02**, 006, arXiv:1906.06352 [hep-ph].

[4] D. Cyncynates and T. Giurgica-Tiron, Structure of the oscillon: The dynamics of attractive self-interaction, *Phys. Rev. D* **103**, 116011 (2021), arXiv:2104.02069 [hep-ph].

[5] M. A. Amin, J. Braden, E. J. Copeland, J. T. Giblin, C. Solorio, Z. J. Weiner, and S.-Y. Zhou, Gravitational waves from asymmetric oscillon dynamics?, *Phys. Rev. D*

**98**, 024040 (2018), arXiv:1803.08047 [astro-ph.CO].

[6] E. Cotner, A. Kusenko, and V. Takhistov, Primordial Black Holes from Inflaton Fragmentation into Oscillons, *Phys. Rev. D* **98**, 083513 (2018), arXiv:1801.03321 [astro-ph.CO].

[7] T. Hiramatsu, E. I. Sfakianakis, and M. Yamaguchi, Gravitational wave spectra from oscillon formation after inflation, *JHEP* **03**, 021, arXiv:2011.12201 [hep-ph].

[8] X.-X. Kou, J. B. Mertens, C. Tian, and S.-Y. Zhou, Gravitational Waves from Fully General Relativistic Oscillon Preheating, (2021), arXiv:2112.07626 [gr-qc].

[9] V. E. Zakharov and A. B. Shabat, Interaction between solitons in a stable medium, *Sov. Phys. JETP* **37**, 823 (1973).

[10] M. J. Ablowitz, D. J. Kaup, A. C. Newell, and H. Segur, Method for solving the sine-gordon equation, *Phys. Rev. Lett.* **30**, 1262 (1973).

[11] N. J. Zabusky and M. D. Kruskal, Interaction of "solitons" in a collisionless plasma and the recurrence of initial states, *Phys. Rev. Lett.* **15**, 240 (1965).

[12] A. Shabat and V. Zakharov, Exact theory of two-dimensional self-focusing and one-dimensional self-modulation of waves in nonlinear media, *Soviet physics JETP* **34**, 62 (1972).

[13] M. Gleiser and A. Sornborger, Longlived localized field configurations in small lattices: Application to oscillons, *Phys. Rev. E* **62**, 1368 (2000), arXiv:patt-sol/9909002.

[14] N. Graham and N. Stamatopoulos, Unnatural Oscillon Lifetimes in an Expanding Background, *Phys. Lett. B* **639**, 541 (2006), arXiv:hep-th/0604134.

[15] M. Gleiser and D. Sicilia, Analytical Characterization of Oscillon Energy and Lifetime, *Phys. Rev. Lett.* **101**, 011602 (2008), arXiv:0804.0791 [hep-th].

[16] P. M. Saffin, P. Tognarelli, and A. Tranberg, Oscillon Lifetime in the Presence of Quantum Fluctuations, *JHEP* **08**, 125, arXiv:1401.6168 [hep-ph].

[17] H.-Y. Zhang, M. A. Amin, E. J. Copeland, P. M. Saffin, and K. D. Lozanov, Classical Decay Rates of Oscillons, *JCAP* **07**, 055, arXiv:2004.01202 [hep-th].

[18] J. Olle, O. Pujolas, and F. Rompineve, Recipes for oscillon longevity, *JCAP* **09**, 015, arXiv:2012.13409 [hep-ph].

[19] P. Dorey, T. Romanczukiewicz, and Y. Shnir, Staccato radiation from the decay of large amplitude oscillons, *Phys. Lett. B* **806**, 135497 (2020), arXiv:1910.04128 [hep-th].

[20] B. C. Nagy and G. Takacs, Collapse instability and staccato decay of oscillons in various dimensions, *Phys. Rev. D* **104**, 056033 (2021), arXiv:2105.01089 [hep-th].

[21] M. Hindmarsh and P. Salmi, Numerical investigations of oscillons in 2 dimensions, *Phys. Rev. D* **74**, 105005 (2006), arXiv:hep-th/0606016.

[22] M. Gleiser and D. Sicilia, A General Theory of Oscillon Dynamics, *Phys. Rev. D* **80**, 125037 (2009), arXiv:0910.5922 [hep-th].

[23] P. Salmi and M. Hindmarsh, Radiation and Relaxation of Oscillons, *Phys. Rev. D* **85**, 085033 (2012), arXiv:1201.1934 [hep-th].

[24] J. T. Gálvez Ghersi and L. C. Stein, Numerical renormalization-group-based approach to secular perturbation theory, *Phys. Rev. E* **104**, 034219 (2021), arXiv:2106.08410 [hep-th].

[25] L. McAllister, E. Silverstein, and A. Westphal, Gravity Waves and Linear Inflation from Axion Monodromy, *Phys. Rev. D* **82**, 046003 (2010), arXiv:0808.0706 [hep-th].

[26] R. Flauger, L. McAllister, E. Pajer, A. Westphal, and G. Xu, Oscillations in the CMB from Axion Monodromy Inflation, *JCAP* **06**, 009, arXiv:0907.2916 [hep-th].

[27] X. Dong, B. Horn, E. Silverstein, and A. Westphal, Simple exercises to flatten your potential, *Phys. Rev. D* **84**, 026011 (2011), arXiv:1011.4521 [hep-th].

[28] W. Jin, R. Brandenberger, and L. Heisenberg, Axion monodromy inflation, trapping mechanisms and the swampland, *Eur. Phys. J. C* **81**, 162 (2021), arXiv:2010.04999 [hep-th].

[29] S. Kasuya, M. Kawasaki, and F. Takahashi, I-balls, *Phys. Lett. B* **559**, 99 (2003), arXiv:hep-ph/0209358.

[30] L. A. Ferreira and W. J. Zakrzewski, The concept of quasi-integrability: a concrete example, *JHEP* **05**, 130, arXiv:1011.2176 [hep-th].

[31] L. A. Ferreira, G. Luchini, and W. J. Zakrzewski, The concept of quasi-integrability, *AIP Conf. Proc.* **1562**, 43 (2013), arXiv:1307.7722 [hep-th].

[32] H. Blas and H. F. Callisaya, Quasi-integrability in deformed sine-Gordon models and infinite towers of conserved charges, *Commun. Nonlinear Sci. Numer. Simul.* **55**, 105 (2018), arXiv:1605.08957 [hep-th].

[33] M. Riesz, L'intégrale de riemann-liouville et le problème de cauchy, *Acta mathematica* **81**, 1 (1949).

[34] P. Virtanen, R. Gommers, T. E. Oliphant, M. Haberland, T. Reddy, D. Cournapeau, E. Burovski, P. Peterson, W. Weckesser, J. Bright, S. J. van der Walt, M. Brett, J. Wilson, K. J. Millman, N. Mayorov, A. R. J. Nelson, E. Jones, R. Kern, E. Larson, C. J. Carey, I. Polat, Y. Feng, E. W. Moore, J. VanderPlas, D. Laxalde, J. Perktold, R. Cimrman, I. Henriksen, E. A. Quintero, C. R. Harris, A. M. Archibald, A. H. Ribeiro, F. Pedregosa, P. van Mulbregt, and SciPy 1.0 Contributors, SciPy 1.0: Fundamental Algorithms for Scientific Computing in Python, *Nature Methods* **17**, 261 (2020).

[35] J. D. Hunter, Matplotlib: A 2d graphics environment, *Computing in Science & Engineering* **9**, 90 (2007).

[36] G. Fodor, P. Forgacs, Z. Horvath, and A. Lukacs, Small amplitude quasi-breathers and oscillons, *Phys. Rev. D* **78**, 025003 (2008), arXiv:0802.3525 [hep-th].

[37] G. Fodor, *A review on radiation of oscillons and oscillations*, Ph.D. thesis, Wigner RCP, Budapest (2019), arXiv:1911.03340 [hep-th].

[38] D. G. Levkov, V. E. Maslov, E. Y. Nugaev, and A. G. Panin, An Effective Field Theory for Large Oscillons, (2022), arXiv:2208.04334 [hep-th].

[39] J. L. Cardy, *Scaling and renormalization in statistical physics*, Cambridge lecture notes in physics (Cambridge Univ. Press, Cambridge, 1996).

[40] M. P. Kennett, *Essential Statistical Physics* (Cambridge University Press, 2020).

[41] G. 't Hooft and M. J. G. Veltman, Regularization and Renormalization of Gauge Fields, *Nucl. Phys. B* **44**, 189 (1972).

[42] M. E. Peskin and D. V. Schroeder, *An Introduction to quantum field theory* (Addison-Wesley, Reading, USA, 1995).

[43] S. Weinberg, *The Quantum theory of fields. Vol. 1: Foundations* (Cambridge University Press, 2005).

[44] P. Bloomfield, *Fourier analysis of time series: an introduction* (John Wiley & Sons, 2004).

[45] M. Hindmarsh and P. Salmi, Oscillons and domain walls, *Phys. Rev. D* **77**, 105025 (2008), arXiv:0712.0614 [hep-th].

[46] J. J. Blanco-Pillado, D. Jiménez-Aguilar, and J. Urrestilla, Exciting the domain wall soliton, *JCAP* **01**, 027,

arXiv:2006.13255 [hep-th].

[47] J. J. Blanco-Pillado, D. Jiménez-Aguilar, J. M. Queiruga, and J. Urrestilla, The dynamics of Domain Wall Strings, (2022), arXiv:2209.12945 [hep-th].

[48] A. V. Frolov, J. T. Gálvez Ghersi, and A. Zucca, Unscreening scalarons with a black hole, *Phys. Rev. D* **95**, 104041 (2017), arXiv:1704.04114 [gr-qc].

[49] J. P. Boyd, *Chebyshev and Fourier Spectral Methods* (Dover Publications, Mineola, NY, 2001).

[50] M. Frigo and S. G. Johnson, The Design and Implementation of FFTW3, *IEEE Proc.* **93**, 216 (2005).

[51] J. C. Butcher, Implicit Runge-Kutta Processes, *Mathematics of Computation* **18**, 50 (1964).

[52] S. G. Johnson, Notes on perfectly matched layers (pmls), *CoRR* **abs/2108.05348** (2021), 2108.05348.